

OPEN ACCESS

A Finite Element Formulation to Three-Dimensionally Resolve Space-Charge Layers in Solid Electrolytes

To cite this article: Stephan Sinzig *et al* 2023 *J. Electrochem. Soc.* **170** 040513

View the [article online](#) for updates and enhancements.

You may also like

- [Enhanced performance of InAs-based interband cascade lasers emitting between 10–13 \$\mu\text{m}\$](#)

Jeremy A Massengale, Yixuan Shen, Rui Q Yang *et al.*

- [Broadly tunable single-mode mid-infrared quantum cascade lasers](#)

Bo Meng and Qi Jie Wang

- [Conservation laws of optical Bloch equations for the tripod scheme - contribution of double dark-state](#)

Jelena Dimitrijevi, Branislav M Jelenkovi and Dušan Arsenovi

Investigate your battery materials under defined force!
The new PAT-Cell-Force, especially suitable for solid-state electrolytes!



- Battery test cell for force adjustment and measurement, 0 to 1500 Newton (0-5.9 MPa at 18mm electrode diameter)
- Additional monitoring of gas pressure and temperature




www.el-cell.com +49 (0) 40 79012 737 sales@el-cell.com

EL-CELL[®]
electrochemical test equipment





A Finite Element Formulation to Three-Dimensionally Resolve Space-Charge Layers in Solid Electrolytes

Stephan Sinzig,^{1,2,z,*}  Thomas Hollweck,¹ Christoph P. Schmidt,^{1,*}  and Wolfgang A. Wall¹ 

¹TUM School of Engineering and Design, Department of Engineering Physics and Computation, Institute for Computational Mechanics, Technical University of Munich, Germany

²TUMint.Energy Research GmbH, 85748 Garching bei München, Germany

All-solid-state batteries are seen as promising candidates to replace conventional batteries with liquid electrolytes in many applications. However, they are not yet feasible for many relevant applications. One particular question of interest is the identification of physical effects inside all-solid-state batteries and their quantitative influence on the performance of the entire battery cell. Simulation models can contribute to answering the aforementioned question by systematic studies, e.g. enabling or disabling certain physical effects. Especially the influence of space-charge layers (SCLs) is heavily discussed in the scientific community. So far, the different length scales of SCLs and the microstructure of a battery cell made a spatial discretization of realistic microstructures with resolved SCLs infeasible. However, thermodynamically consistent continuum models which are applied to simplified geometries are already established in the literature. In this work, we propose a model that enables the prediction of the spatial development of SCLs within geometrically resolved microstructures by exploiting that effects in SCLs are predominantly one-dimensional. With the proposed approach it is possible to quantify the geometric influence of realistic microstructures on the formation process of SCLs. SCLs in realistic microstructures remarkably differ from SCLs computed with simplified one-dimensional models which are already established in the literature.

© 2023 The Author(s). Published on behalf of The Electrochemical Society by IOP Publishing Limited. This is an open access article distributed under the terms of the Creative Commons Attribution 4.0 License (CC BY, <http://creativecommons.org/licenses/by/4.0/>), which permits unrestricted reuse of the work in any medium, provided the original work is properly cited. [DOI: 10.1149/1945-7111/acc692]



Manuscript submitted January 14, 2023; revised manuscript received March 3, 2023. Published April 17, 2023.

Research activity has strongly increased in recent years to improve both the energy and power densities of batteries. Especially, lithium-ion batteries are nowadays seen as the superior battery technology for many applications,¹ especially for electric vehicles. It is foreseeable, that conventional lithium-ion batteries with liquid electrolytes will reach their physical limit soon. All-solid-state batteries could theoretically overcome the drawbacks of conventional lithium-ion batteries with liquid electrolytes. Some of the advantages of all-solid-state batteries are their possibility for high power densities, facilitating of lithium metal anodes, thus achieving high energy densities, and ensuring high safety standards due to the non-flammability of many solid electrolytes.^{2–4} However, they still require more research effort to establish them for various real-world applications. While experimental research is already well-established in the field of electrochemistry, simulative investigations become more prominent to rapidly evaluate the influence of different operating scenarios, quantifying the influence of certain physical effects, or testing the combination of different materials. Profound predictions of the behavior of a battery cell require models that are based on fundamental physics and are solved in a mathematically consistent manner.

The formation of regions where charges separate, i.e. double layers for liquid electrolytes⁵ and space-charge layers (SCLs) for solid electrolytes,⁶ is known for decades. However, their influence in terms of resistance and capacitance on the entire battery cell is heavily discussed in the literature,⁷ ranging from rather negligible^{8,9} to important.^{10–12} We do not claim to give a full overview of the physical phenomena inside SCLs but refer the reader to the literature, e.g. in Ref. 13 and summarize only the key aspects. SCLs are small regions inside the solid electrolyte, that form close to the electrodes. Inside these regions, separation of charges is observable (e.g. in Refs. 14, 15), as shown in various experiments.^{16–22} Due to the different chemical potentials of two materials in contact, charge carriers will redistribute to form either an accumulation layer or a depletion layer until equilibrium is reached.²³ SCLs occur at all interfaces of a battery cell where two materials with different chemical potentials are in contact. They

occur especially at the interface between the solid electrolyte and the electrodes, and at internal interfaces inside the solid electrolyte.²⁴

Simulation models can contribute to the mentioned discussion of the influence of SCLs on the entire battery cell. Of course, a simulation model can never cover all physical effects, that occur inside an all-solid-state battery but needs to be tailored to the specific question that it should answer. In the scientific community, different modeling approaches are available to incorporate the effect of SCLs into a model, each with a different focus: Atomistic models (e.g. in Refs. 25, 26), DFT models (e.g. in Refs. 11, 27), kinetic Monte Carlo models (e.g. in Ref. 28), or continuum models. In light of the following sections, we want to elaborate more on continuum models, as the other models can only be applied to domains with dimensions in the range of nanometers due to computational limitations and thus, not to geometries representing realistic microstructures. Continuum models can be further subdivided into: Phenomenological models, which modify known equations e.g. from liquid electrolytes to include the effects of solid electrolytes (e.g. in Refs. 29–31), zero-dimensional models, that resolve a complex geometric microstructure and add e.g. a capacitor to the interface to represent SCLs (e.g. in Refs. 32–34), and one-dimensional models, that spatially resolve the shape of SCLs between two electrodes (e.g. in Refs. 35, 36). As all models, the outlined models have different limitations that can be significant for relevant questions. Phenomenological models do not ensure positive entropy production and are thus thermodynamically not consistent or neglect the transient development of the SCL, zero-dimensional models cannot resolve the spatial shape of SCLs, and one-dimensional models neglect the inhomogeneous geometric influence, which can be significant as we will show in this work. For completeness, we want to state that also the chosen model^{35,36} has limitations originating from the atomistic nature of the charges that make up the SCL. The model neglects Coulomb interaction between Li-defects and impurities of the crystal lattice.⁷ The interaction of discretized sites at high concentrations is not well described by bulk dielectric screening. Additionally, the model does not account for the electronic structure of the electrolyte (see e.g. in Ref. 11 for details) which can be important in the near electrode region. However, incorporating these effects into a continuum model is beyond the scope of this work.

Especially the different length scales (≈ 10 – 100 nm¹⁸) of SCLs and realistic microstructures (≈ 100 μ m) are currently hindering a

*Electrochemical Society Student Member.

^zE-mail: stephan.sinzig@tum.de

three-dimensionally resolved solution of the SCLs in realistic microstructures. A three-dimensional mesh, as needed for the discretization of the continuous model, e.g. with the finite element method, would require mesh cells with a size of about 1 nm to capture gradients within the thin layer. This would exceed currently available computational resources if realistic microstructures would be discretized with the required fineness, resulting in the order of one billion nodes of a discretization mesh.

In this work, we introduce a novel approach that allows resolving and incorporating SCLs within geometrically complex microstructures. The approach is motivated by the observation, that SCLs develop in regions close to the electrodes and are predominantly one-dimensional due to the perpendicular electric field on equipotential surfaces, i.e. perfectly electronic conducting electrodes. In the remaining part of the solid electrolyte, the condition of local charge neutrality holds.¹⁵ By using different discretizations in SCL regions and outside of SCL regions we propose a solution to the unsolved challenge to resolve SCLs in realistic microstructures. Based on the observation of predominant one-dimensional effects in SCLs we discretize the domain in the vicinity of the electrodes in one dimension, while it is three-dimensionally discretized outside of the SCL region. This reduces the computational effort significantly because the mesh size outside of the SCL region can be adapted according to the dimensions of the microstructure, while the one-dimensional discretization in the SCL region can be adapted to the shape of the SCL. Consequently, the computational effort reduces to a manageable size. We base the continuous SCL model on the work reported in Refs. 35, 36, which guarantees positive production of entropy and is formulated in the three-dimensional space. However, our proposed discretization scheme is not attached to this model but is conceptually applicable to any other continuum model for SCLs. Additionally, we reduce the computational effort, by enforcing the condition of constant concentrations to regions outside of the SCL.

This work is outlined as follows: We begin with recalling a continuous approach to model SCLs including physically meaningful boundary and initial conditions. Afterwards, we simplify the model outside of the SCL regions by enforcing constant concentrations. Based on this, we introduce a novel approach for a consistent coupling of SCL regions and regions outside of the SCL. Subsequently, we present the numerical incorporation of the coupling of the SCL regions and regions outside of the SCL and add remarks on an efficient solution strategy for this system. Moreover, we present results computed with the proposed coupling approach to compare our solution with one-dimensional models, to find a quantitative measure for the size of the SCL region, to validate conservation principles, to quantify the quality of the proposed approach by defining approximation errors, and to show the applicability to large systems that represent realistic microstructures.

To our knowledge, this work is the first to show results for spatially resolved SCLs within realistic microstructures.

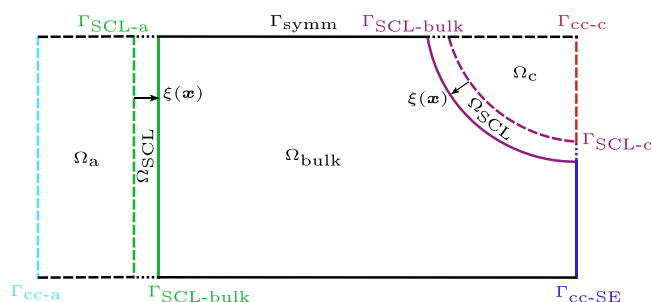


Figure 1. Schematic sketch of the computational domain. The domain is split into subdomains Ω_i and surfaces Γ_{i-j} denoting the interface between the domains Ω_i and Ω_j .

Continuum Model for Solid Electrolytes Including SCLs

In this section, we present a continuum model for SCLs by splitting the geometry of the solid electrolyte into an SCL region close to the electrodes and the remaining domain. We summarize a thermodynamically consistent model for solid electrolytes, which is already established in the literature. Subsequently, we define different assumptions for the two domains and apply them to the thermodynamically consistent model. Afterwards, we elaborate on the coupling between both domains and discuss the approximation errors that we introduce by our proposed approach.

Geometric definitions and nomenclature.—Before presenting the equations that define the model for the solid electrolyte, we need to define the geometric setup as shown in Fig. 1 that schematically sketches both electrodes and the solid electrolyte. The focus of this work is on the domain of the solid electrolyte Ω_{SE} where the development of SCLs is expected, as we do not consider charge separation in the electrodes in this work. The domain of the solid electrolyte is split into a part where we expect SCLs to develop Ω_{SCL} and into the bulk domain Ω_{bulk} : $\Omega_{SE} = \Omega_{SCL} \cup \Omega_{bulk}$. The electrodes Ω_{ed} are subdivided into the anode Ω_a and the cathode Ω_c : $\Omega_{ed} = \Omega_a \cup \Omega_c$. Their boundaries are drawn by dashed lines to indicate, that we do not solve any equations inside these domains within this work. Instead, we focus on the solid electrolyte as we are only interested in the SCLs that form at the interface between the electrolyte and the electrodes. Thus, we do not resolve SCLs at grain boundaries inside the solid electrolyte. However, their incorporation would be methodologically identical.

We define surfaces as intersections of domains or outer boundaries. At first, we define the intersection between the bulk domain of the solid electrolyte Ω_{bulk} and the SCL domains Ω_{SCL} as $\Gamma_{SCL-bulk}$. The intersection between the electrodes Ω_{ed} and the SCL domain Ω_{SCL} is defined as Γ_{SCL-ed} . All boundaries in the lateral direction of the battery cell are model boundaries, where symmetry assumptions are made and the according boundary conditions are applied. They are denoted with Γ_{symm} . For completeness, we define outer boundaries to the current collectors Γ_{cc-a} , Γ_{cc-c} , and Γ_{cc-SE} where Γ_{cc-SE} includes the boundaries of both the SCL domain Ω_{SCL} and the bulk domain Ω_{bulk} of the solid electrolyte.

Finally, a natural coordinate $\xi(x)$ is introduced perpendicular to $\Gamma_{SCL-bulk}$ which is restricted to Ω_{SCL} . Its direction is defined from the electrodes to the electrolyte, with the origin at the electrode. Consequently, it is a function of the location x .

Thermodynamically consistent model for solid electrolytes including SCLs.

—We use the approach developed in Ref. 35 and later extended in Ref. 36 to model the electrochemical transport phenomena in solid electrolytes. This approach is thermodynamically consistent, i.e. a positive production rate of entropy is guaranteed. The key aspects of the approach as well as the used symbols are summarized in the Appendix A and the governing equations are

$$\frac{\partial c_+}{\partial t} + \nabla \cdot N_+ = 0 \quad \text{in } \Omega_{SE}, \quad [1]$$

$$\frac{\partial q}{\partial t} + \nabla \cdot \left(z_+ F N_+ - \epsilon_0 \chi \frac{\partial \nabla \Phi}{\partial t} \right) = 0 \quad \text{in } \Omega_{SE}, \quad [2]$$

$$-\nabla \cdot (\epsilon \nabla \Phi) = q_F \quad \text{in } \Omega_{SE}, \quad [3]$$

$$N_+ = -D_+ \nabla c_+ - \frac{\sigma}{z_+ F} \nabla \Phi \quad \text{in } \Omega_{SE}. \quad [4]$$

A physically meaningful (i.e. no violation of conservation properties) and mathematically consistent set of boundary conditions needs to be defined to obtain a well-posed system. The shape of the SCLs

is determined by the boundary conditions applied to the interface between the solid electrolyte and the electrodes $\Gamma_{\text{SCL-ed}}$. In the remaining Sections of this work, we assume blocking electrodes which lead to Dirichlet boundary conditions for the electric potential and homogeneous Neumann boundary conditions for the concentration of cations on the interface

$$\Phi = \hat{\Phi} \quad \text{on } \Gamma_{\text{SCL-ed}}, \quad [5]$$

$$N_+ \cdot \mathbf{n} = 0 \quad \text{on } \Gamma_{\text{SCL-ed}}. \quad [6]$$

For completeness, we define homogeneous Neumann boundary conditions as well for all quantities on Γ_{Symm} and note that all boundary conditions have to satisfy global charge neutrality, namely $\int_{\Omega_{\text{SE}}} q(\mathbf{x}, t) d\Omega = 0 \quad \forall t$.

For the transient equations, we define initial conditions that represent an unpolarized solid electrolyte. This results in bulk concentration for anions c_- and cations c_+ , and thus implicitly zero total charge q

$$c_+(\mathbf{x}, t = 0) = c_-(\mathbf{x}, t = 0) = c_{\text{bulk}}, \quad [7]$$

$$q(\mathbf{x}, t = 0) = 0. \quad [8]$$

Assumption of constant concentrations outside of the SCL region.—For the derivation of a model of the solid electrolyte outside of the SCL region, we start with the fundamental assumption

$$c_+ = c_- = c_{\text{bulk}} = \text{const.} \quad \text{in } \Omega_{\text{bulk}}. \quad [9]$$

This is a reasonable assumption for transference numbers close to unity if the local electroneutrality condition is satisfied.^{7,37} As a direct consequence this assumption implies $\frac{\partial c_+}{\partial t} = 0$ and $\nabla c_+ = 0$. Within this work, we keep the dielectric permeability independent of any excitation frequencies, i.e. $\epsilon = \text{const.}$ The assumption in Eq. 9 ensures that no free charge (see Eq. A.2) accumulates, as positive and negative charges sum up to zero $q_{\text{F}} = 0$.

In the following, we will show that those assumptions simplify the system of equations outlined before to a Laplace equation for the electric potential $\Delta\Phi = 0$. First, we simplify the constitutive equation for the flux of cations in Eq. 4. The diffusive term related to the gradient of the concentration vanishes

$$N_+ = -\frac{\sigma}{z_+F} \nabla\Phi. \quad [10]$$

Moreover, the transport properties become constants with respect to the cation concentration, namely the ionic conductivity and the diffusion coefficient

$$\sigma = (z_+F)^2 \mathcal{L}_{++} (1 - (c_{\text{max}} - c_{\text{bulk}})c_{\text{bulk}} \Delta\nu), \quad [11]$$

$$D_+ = \mathcal{L}_{++} RT \frac{c_{\text{max}}}{(c_{\text{max}} - c_{\text{bulk}})c_{\text{bulk}}}. \quad [12]$$

By using the absence of free charge Ω_{bulk} , Eq. 3 simplifies to $\nabla \cdot (\epsilon \nabla\Phi) = 0$, and by using constant dielectric permeability ϵ it simplifies further to the Laplace equation

$$\Delta\Phi = 0 \quad \text{in } \Omega_{\text{bulk}}. \quad [13]$$

Furthermore, Eq. 1 reduces to $\nabla \cdot \left(-\frac{\sigma}{z_+F} \nabla\Phi \right) = 0$ by using that the temporal derivative of the cation concentration is zero and by substituting the expression for the flux of cations N_+ . All prefactors are constant in this expression, such that this equation reduces to $\Delta\Phi = 0$ as well.

Finally, we substitute all findings into Eq. 2 and apply the divergence operator on both terms inside the brackets

$$\frac{\partial q}{\partial t} + \left(-\sigma \Delta\Phi - \epsilon_0 \chi \frac{\partial \Delta\Phi}{\partial t} \right) = 0. \quad [14]$$

As shown before, the Laplacian of Φ will evaluate to zero, such that only the temporal derivative of the total charge density $\frac{\partial q}{\partial t}$ remains. The total charge density q is composed by summing up the free charge density q_{F} and the bound charge density q_{B} . For the first, we already know that it is zero, while the latter is defined as $q_{\text{B}} = \epsilon_0 \chi \Delta\Phi$. Again, we make use of the Laplacian of Φ to be zero leading to $q_{\text{B}} = 0$. Finally, we can conclude that $q = 0$. Obviously, this equation ($0 = 0$) is implicitly fulfilled. This means, that from the entire set of equations, we only need to solve for the Laplacian of Φ to be zero in Ω_{bulk} .

Assumption of one-dimensionality inside the SCL region.—The key aspect of this work is to propose a model that can spatially resolve the effect of SCLs in realistic microstructures by reducing the required computational effort. We do this by assuming, that all spatial derivatives inside Ω_{SCL} that are tangential to the interface $\Gamma_{\text{SCL-bulk}}$ vanish

$$(\nabla\Psi - (\nabla\Psi \cdot \mathbf{n})\mathbf{n}) \cdot \mathbf{n} = 0 \quad \text{in } \Omega_{\text{SCL}}, \quad [15]$$

for any scalar quantity Ψ and the vector \mathbf{n} being normal to the interface $\Gamma_{\text{SCL-bulk}}$ with length one. This assumption is motivated by the observable main characteristics of SCLs that are predominantly one-dimensional. The one-dimensionality is caused by the electric field $\mathbf{E} = -\nabla\Phi$ which has to be perpendicular to equipotential, i.e. ideally conducting surfaces $\nabla\Phi \cdot \mathbf{n} = \|\nabla\Phi\|$ as a limit assumption for the high conductivity of many electrode materials. Furthermore, we distinguish between the steady state and the transient state for blocking electrodes. In the steady state, the flux of cations vanishes, and Eq. 4 simplifies to $\nabla c_+ = -\frac{\sigma}{D_+ z_+ F} \nabla\Phi$. Consequently, the gradient of the cation concentration in the steady state is normal to the surface as well. Thus, the electric potential and the concentration are constant on this surface. Now, we conclude that the electric potential and the concentration at an infinitesimal distance from the surface are equal as well, due to the constant values at the surface and normal gradients with uniform magnitude. This surface with an infinitesimal distance forms another surface with uniform electric potential and concentration. Repeating this thought experiment reveals that the gradient of the electric potential and the concentration is normal to the surface throughout the entire SCL domain, i.e. that all gradients remain parallel to the normal of the surface.

In the transient state, the tangential component of the flux of cations can have non-zero values but remain comparably small as we will show in this work.

Consequently, the partial differential equations as outlined before are reduced to one-dimensional equations. Inside the remaining part of the geometrically complex solid electrolyte Ω_{bulk} , no further constraint to the gradient is given, such that the equations are resolved in all three dimensions of space. Considering this, we arrive at a set of equations inside both the SCL domain Ω_{SCL} and the bulk domain Ω_{bulk}

$$\Delta\Phi_{\text{bulk}} = 0 \quad \text{in } \Omega_{\text{bulk}}, \quad [16]$$

$$\frac{\partial c_{\text{SCL}}}{\partial t} + \frac{\partial N_{\text{SCL}}}{\partial \xi} = 0 \quad \text{in } \Omega_{\text{SCL}}, \quad [17]$$

$$\frac{\partial q_{\text{SCL}}}{\partial t} + \frac{\partial \left(zFN_{\text{SCL}} - \epsilon_0 \chi \frac{\partial \left(\frac{\partial \Phi_{\text{SCL}}}{\partial \xi} \right)}{\partial t} \right)}{\partial \xi} = 0 \text{ in } \Omega_{\text{SCL}}, \quad [18]$$

$$-\frac{\partial \left(\epsilon \frac{\partial \Phi_{\text{SCL}}}{\partial \xi} \right)}{\partial \xi} = q_{\text{F}} \quad \text{in } \Omega_{\text{SCL}}, \quad [19]$$

$$N_{\text{SCL}} = -D \frac{\partial c_{\text{SCL}}}{\partial \xi} - \frac{\sigma}{zF} \frac{\partial \Phi_{\text{SCL}}}{\partial \xi}, \quad [20]$$

where we abbreviated the cation concentration c_+ with c , the flux of cations N_+ with N , the charge number z_+ with z , and the diffusion coefficient D_+ with D , as from now on the cation concentration mathematically is the only unknown concentration. Additionally, we distinguish between quantities in the bulk domain and in the SCL domain by assigning the respective subscript. In the following, we do not solve for the total charge q_{SCL} in Eq. 18, as it is not an independent variable in the case of blocking electrodes and can simply be post-processed from the electric potential and the cation concentration.

Coupling regions inside and outside of the SCL.—At the transition from the bulk domain to the SCL domain $\Gamma_{\text{SCL-bulk}}$ we require continuity between all primary variables, i.e. the concentration, and the electric potential. Additionally, conservation properties need to be ensured. The first requirement is fulfilled by requesting

$$\Phi_{\text{SCL}} = \Phi_{\text{bulk}} \quad \text{on } \Gamma_{\text{SCL-bulk}}, \quad [21]$$

$$c_{\text{SCL}} = c_{\text{bulk}} \quad \text{on } \Gamma_{\text{SCL-bulk}}. \quad [22]$$

The second requirement can be incorporated by enforcing consistent coupling fluxes between two domains. While the flux inside the three-dimensional bulk domain is a vector, the flux inside the one-dimensional SCL domain is treated as a scalar. Thus, the flux inside the bulk domain needs to be projected in the direction normal to the interface implying the one-dimensional SCL domain to be perpendicular to the coupling surface $\Gamma_{\text{SCL-bulk}}$

$$N_{\text{bulk}} \cdot \mathbf{n} = N_{\text{SCL}} \quad \text{on } \Gamma_{\text{SCL-bulk}}, \quad [23]$$

$$\mathbf{i}_{\text{bulk}} \cdot \mathbf{n} = i_{\text{SCL}} \quad \text{on } \Gamma_{\text{SCL-bulk}}. \quad [24]$$

Geometric approximation of realistic microstructures.—We define the bulk domain of the solid electrolyte as $\Omega_{\text{bulk}} = \Omega_{\text{SE}}$ and the SCL domain as $\Omega_{\text{SCL}} = \Gamma_{\text{SCL-bulk}} \times l_{\text{SCL}}$. Here, l_{SCL} is an estimation of the thickness of the SCL and $l_{\text{SCL}} \ll l_{\text{SE}}$, with l_{SE} being a typical length scale of the solid electrolyte. Note, that this approximation slightly enlarges the original geometry.

Approximation errors introduced by the coupling approach.—By coupling the one-dimensional and the three-dimensional domains, we introduce three types of approximation errors to the system. They serve as a measure to quantify the quality of the proposed approach:

1. **Model error.** The model for the bulk domain is derived from the thermodynamically consistent model for SCLs based on the assumption $c_+ = c_- = c_{\text{bulk}}$. Thus, the error introduced by the assumption scales with $\epsilon_{\text{err}} = c_+ - c_{\text{bulk}}$. It is negligible if the SCL domain is chosen large enough as the concentration converges toward the bulk concentration for great distances from $\Gamma_{\text{SCL-ed}}$.

2. **Geometric error.** By adding a thin layer representing the SCL domain we modify the geometry and thus enlarge the geometric dimensions of the solid electrolyte. Effectively, this results in a slightly larger resistance of the solid electrolyte. However, we select the thickness of the additional layer $l_{\text{SCL}} \ll l_{\text{SE}}$ which means that the additional resistance, which scales with the length of the solid electrolyte, is negligible. In case the aforementioned condition is not valid anymore, it is possible to reduce the size of the bulk domain to compensate for the additional thin layer representing the SCL.

3. **Compatibility error.** The one-dimensional model inside the SCL domain can only capture gradients in the direction normal to $\Gamma_{\text{SCL-bulk}}$. Gradients parallel to $\Gamma_{\text{SCL-bulk}}$ on equipotential surfaces occur in the transient state but cannot cause a flux in the one-dimensional model. Again, this error is comparably small as long as $l_{\text{SCL}} \ll l_{\text{SE}}$. Exemplarily, this can be shown by a Taylor expansion of the electric potential for a two-dimensional geometry in polar coordinates (r, θ) to capture the curvature of the equipotential surface:

$$\begin{aligned} \Phi(r, \theta) = \Phi(\mathbf{0}) + \left[\frac{\partial \Phi}{\partial r} \quad \frac{1}{r} \frac{\partial \Phi}{\partial \theta} \right] \Big|_0 \begin{bmatrix} r \\ \theta \end{bmatrix} \\ + \frac{1}{2} [r \quad \theta] \begin{bmatrix} \frac{\partial^2 \Phi}{\partial r^2} & \frac{\partial^2 \Phi}{\partial r \partial \theta} - \frac{1}{r} \frac{\partial \Phi}{\partial \theta} \\ \frac{\partial^2 \Phi}{\partial r \partial \theta} - \frac{1}{r} \frac{\partial \Phi}{\partial \theta} & \frac{\partial^2 \Phi}{\partial \theta^2} + \frac{1}{r} \frac{\partial \Phi}{\partial r} \end{bmatrix} \Big|_0 \begin{bmatrix} r \\ \theta \end{bmatrix} + \mathcal{O}^3(r, \theta) \end{aligned} \quad [25]$$

Due to the equipotential surface, the derivatives $\frac{\partial \Phi}{\partial \theta}$ and $\frac{\partial^2 \Phi}{\partial \theta^2}$ vanish. The compatibility error scales with derivatives the reduced dimensional model cannot capture, i.e. derivatives w.r.t. θ , and thus w.r.t. $\frac{\partial^2 \Phi}{\partial r \partial \theta} \Big|_0 r\theta$. Therefore, the distance to the equipotential surface must be minimal to reduce the compatibility error.

We conclude, that the domain of the SCL should be as large as possible to reduce the first approximation error, while it should be as small as possible, to reduce the other two approximation errors. We will present concepts on how to choose the size of the SCL domain.

Numerical Treatment of The SCL Model

In this Section we want to present the discretization schemes in space and time we used to discretize the continuous equations. Furthermore, we show the incorporation of the coupling conditions between the bulk domain and the SCL domain into the discretized system of equations. Afterwards, we discuss the required constraint enforcement and the applied solution techniques.

Discretization in time.—The equation for the bulk domain is stationary, while the set of equations for the SCL domain contains time derivatives, namely the temporal derivative of the concentration. Thus, only the mass conservation equation in the SCL domains is discretized in time. It is not the aim of this work to rewrite in all detail the steps for discretizing the time-continuous equations. For brevity, the main steps of the One-Step-Theta method which is used in this work are recaptured. It is used to discretize first-order differential equations of the type

$$\frac{\partial c_{\text{SCL}}}{\partial t} = \text{fn}(c_{\text{SCL}}, \mathbf{x}), \quad [26]$$

in time for $t \in [t_0, t_{\text{end}}]$. The underlying discretization scheme can be expressed as

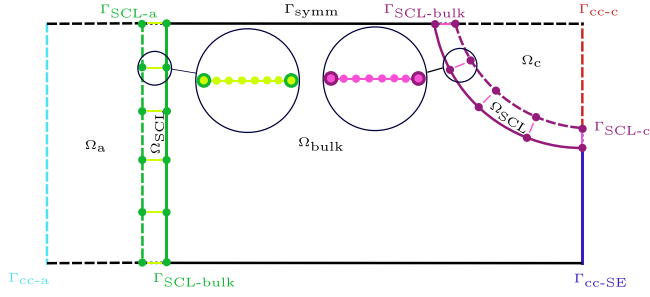


Figure 2. Schematic sketch of the discrete coupling between the two domains with different dimensions of space.

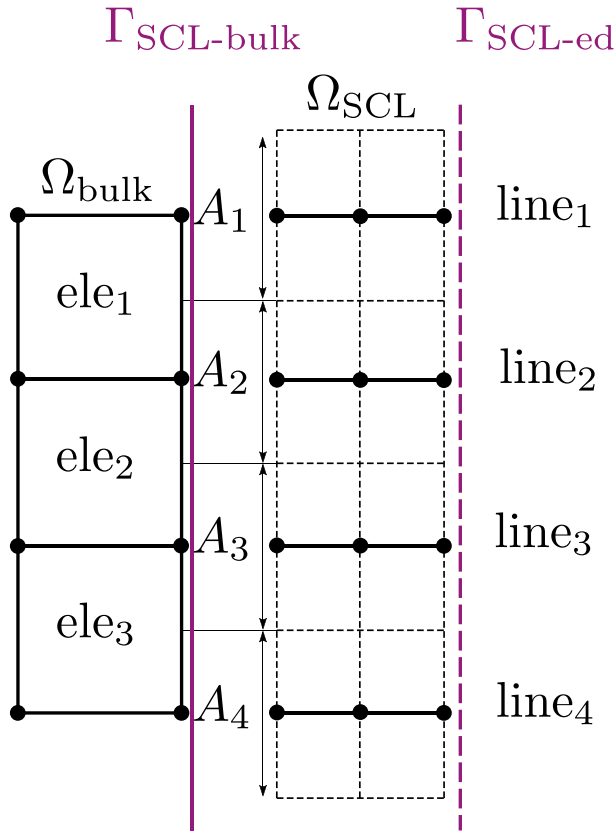


Figure 3. Projected one-dimensional discretization on the two-dimensional interface. Scaling of the equations in the SCL domain with the projected area A_i guarantees the conservation properties across the interface $\Gamma_{\text{SCL-bulk}}$.

$$\frac{\partial c_{\text{SCL}}}{\partial t} \approx \frac{c_{\text{SCL}}^{n+1} - c_{\text{SCL}}^n}{\Delta t} = \theta \text{fn}(c_{\text{SCL}}^{n+1}, \mathbf{x}) + (1 - \theta) \text{fn}(c_{\text{SCL}}^n, \mathbf{x}), \quad [27]$$

with c_{SCL}^n and c_{SCL}^{n+1} being the values of c_{SCL} at time steps t_n and t_{n+1} , with possibly non-uniform values of the time step size Δt . Choosing $\theta = 0.5$ represents the well-established implicit Crank-Nicolson scheme of second-order accuracy.

Discretization in space.—We use the finite element method to discretize the set of partial differential equations in space for both the bulk domain Ω_{bulk} and the SCL domain Ω_{SCL} . While the bulk domain is discretized in all three dimensions of space, the domain for the SCL is only discretized in one dimension. Consequently, the number of unknowns of the spatial discretization reduces significantly, as a fine discretization in only one direction is required.

Again, we do not aim to walk the reader through all steps of the discretization scheme of the finite element method but want to focus on the main aspects. First, we derive the weak form of equations 16 to 20 by multiplication with an arbitrary test function w , integration over the respective domain, and transforming derivatives of second order in space to the test function w by applying the chain rule of divergence and Gauß divergence theorem. Afterwards, we discretize the geometry (\mathbf{x}), the test functions (w), and the solution variables (Φ_{bulk} , c_{SCL} , Φ_{SCL}) with the same shape functions. This means that $\Psi = N\hat{\Psi}$, with $\Psi \in \{\mathbf{x}, w, \Phi_{\text{bulk}}, c_{\text{SCL}}, \Phi_{\text{SCL}}\}$ represents the vector of all variables, N the matrix of corresponding size containing the shape functions, and $\hat{\Psi}$ the vector of the discretized variables. Throughout this work, we use linear shape functions for the matrix N . Finally, we arrive at a set of nonlinear, algebraic equations

$$\mathbf{R}_{\Phi}^{\text{bulk}}(\Phi_{\text{bulk}}^{n+1}) = \mathbf{0}, \quad [28]$$

$$\mathbf{R}_c^{\text{SCL}}(c_{\text{SCL}}^{n+1}, \Phi_{\text{SCL}}^{n+1}) = \mathbf{0}, \quad [29]$$

$$\mathbf{R}_{\Phi}^{\text{SCL}}(c_{\text{SCL}}^{n+1}, \Phi_{\text{SCL}}^{n+1}) = \mathbf{0}, \quad [30]$$

where Φ_{bulk}^{n+1} , c_{SCL}^{n+1} , and Φ_{SCL}^{n+1} denote the vector-organized nodal values of the primary variables.

Solution of the algebraic nonlinear system of equations.—The set of nonlinear equations is solved by the Newton-Raphson scheme. Both, the primary variables and the residuals are combined into global vectors $\omega^{n+1} = [\Phi_{\text{bulk}}^{n+1}, c_{\text{SCL}}^{n+1}, \Phi_{\text{SCL}}^{n+1}]^T$ and $\mathbf{R} = [\mathbf{R}_{\Phi}^{\text{bulk}}, \mathbf{R}_c^{\text{SCL}}, \mathbf{R}_{\Phi}^{\text{SCL}}]^T$. This allows defining the Newton-Raphson scheme as

$$\omega_{i+1}^{n+1} = \left(\frac{\partial \mathbf{R}}{\partial \omega^{n+1}} \Big|_i \right)^{-1} \mathbf{R}_i + \omega_i^{n+1}, \quad [31]$$

where the inverse of the matrix $\frac{\partial \mathbf{R}}{\partial \omega^{n+1}} \Big|_i$ is of course not computed. Instead, the system $\frac{\partial \mathbf{R}}{\partial \omega^{n+1}} \Big|_i \Delta \omega_{i+1}^{n+1} = \mathbf{R}_i$ is solved using a linear solver, with $\Delta \omega_{i+1}^{n+1} = \omega_{i+1}^{n+1} - \omega_i^{n+1}$. The matrix $\frac{\partial \mathbf{R}}{\partial \omega^{n+1}} \Big|_i$ can be written as

$$\begin{aligned} & \left[\begin{array}{ccc} \frac{\partial \mathbf{R}_{\Phi}^{\text{bulk}}}{\partial \Phi_{\text{bulk}}} & \mathbf{0} & \mathbf{0} \\ \mathbf{0} & \frac{\partial \mathbf{R}_c^{\text{SCL}}}{\partial c_{\text{SCL}}} & \frac{\partial \mathbf{R}_c^{\text{SCL}}}{\partial \Phi_{\text{SCL}}} \\ \mathbf{0} & \frac{\partial \mathbf{R}_{\Phi}^{\text{SCL}}}{\partial c_{\text{SCL}}} & \frac{\partial \mathbf{R}_{\Phi}^{\text{SCL}}}{\partial \Phi_{\text{SCL}}} \end{array} \right] \Big|_i \\ & = \left[\begin{array}{ccc} \mathbf{K}_{\Phi, \Phi}^{\text{bulk}} & \mathbf{0} & \mathbf{0} \\ \mathbf{0} & \mathbf{K}_{c, c}^{\text{SCL}} & \mathbf{K}_{c, \Phi}^{\text{SCL}} \\ \mathbf{0} & \mathbf{K}_{\Phi, c}^{\text{SCL}} & \mathbf{K}_{\Phi, \Phi}^{\text{SCL}} \end{array} \right] \Big|_i = \mathbf{K}_i. \end{aligned} \quad [32]$$

For brevity, we summarize the expressions for the single blocks of the matrix by introducing submatrices $\mathbf{K}_{\Psi_1, \Psi_2}^{\Omega}$.

Incorporation of the coupling by constraint enforcement.—In Fig. 2 we show the discrete coupling scheme between the bulk domain and the SCL domain. The bulk domain Ω_{bulk} is discretized with standard finite elements for three-dimensional spaces, meaning hexahedrals or tetrahedrals. By their choice, the surface discretization of the interface $\Gamma_{\text{SCL-bulk}}$ is determined, namely by quadrilaterals

and triangular. We connect the nodes on $\Gamma_{\text{SCL-bulk}}$ and $\Gamma_{\text{SCL-ed}}$ by introducing a one-dimensional discretization consisting of line elements to discretize Ω_{SCL} . The mesh of the one-dimensional discretization can be much finer compared to the three-dimensional mesh in Ω_{bulk} .

The coupling conditions derived before will now be imposed on the linear system of equations to couple the three-dimensional discretization in Ω_{bulk} with the one-dimensional discretization in Ω_{SCL} . At first, we consider the requirement of conservation across the coupling interface. Therefore, we assign an area A_i to each one-dimensional SCL discretization to extend the discretization to all three dimensions of space (see Fig. 3) which is consistent with the chosen linear shape functions and could be extended to higher-order shape functions. For the linear shape functions, this corresponds to a piecewise constant behavior of the SCL domain in the tangential direction of the interface $\Gamma_{\text{SCL-bulk}}$. Subsequently, we scale both the residual \mathbf{R}^{SCL} and the linearization matrix \mathbf{K}^{SCL} of the SCL domain with the projected areas A_i . We organize the projected areas A_i in a vector and evaluate them by integrating the shape functions at the interface over the constant value one: $\mathbf{A} = \mathbb{A}_{\text{ele}} \int_{\Gamma_{\text{coup,ele}}} N d\Gamma$, with

the assembly operator \mathbb{A}_{ele} . This results in $\mathbf{R}_{\Psi}^{\text{SCL,coup}} = \mathbf{R}_{\Psi}^{\text{SCL}} \mathbf{A}$ and $\mathbf{K}_{\Psi_1, \Psi_2}^{\text{SCL,coup}} = \mathbf{K}_{\Psi_1, \Psi_2}^{\text{SCL}} \mathbf{A}$, with “.” denoting the operator for row-wise multiplication.

Now, we can enforce the requirement of continuity between the bulk domain and the SCL domain. This is achieved by (a) splitting the primary variables into coupled variables Ψ_{coup} and interior variables Ψ_i , (b) further subdividing the coupled variables in accordance with conventions into “slave” on the SCL side and “master” on the bulk side, labeled with “s” and “m” respectively, (c) introducing Lagrangian multipliers to enforce the constraint of continuity $\Psi_{\text{bulk}} = \Psi_{\text{SCL}}$ at $\Gamma_{\text{SCL-bulk}}$, and (d) applying a condensation scheme to remove the Lagrangian multipliers as well as the slave-side interface variables from the system of equations defining the final linear system of equations

$$\begin{aligned} & \begin{bmatrix} \mathbf{K}_{\Phi_i, \Phi_i}^{\text{bulk}} & \mathbf{K}_{\Phi_i, \Phi_m}^{\text{bulk}} & \mathbf{0} & \mathbf{0} \\ \mathbf{K}_{\Phi_m, \Phi_i}^{\text{bulk}} & \mathbf{K}_{\Phi_m, \Phi_m}^{\text{bulk}} + \mathbf{K}_{\Phi_s, \Phi_s}^{\text{SCL}} \mathbf{A} & \mathbf{K}_{\Phi_s, c}^{\text{SCL}} \mathbf{A} & \mathbf{K}_{\Phi_s, \Phi_i}^{\text{SCL}} \mathbf{A} \\ \mathbf{0} & \mathbf{K}_{c, \Phi_s}^{\text{SCL}} \mathbf{A} & \mathbf{K}_{c, c}^{\text{SCL}} \mathbf{A} & \mathbf{K}_{c, \Phi_i}^{\text{SCL}} \mathbf{A} \\ \mathbf{0} & \mathbf{K}_{\Phi_i, \Phi_s}^{\text{SCL}} \mathbf{A} & \mathbf{K}_{\Phi_i, c}^{\text{SCL}} \mathbf{A} & \mathbf{K}_{\Phi_i, \Phi_i}^{\text{SCL}} \mathbf{A} \end{bmatrix} \begin{bmatrix} \Delta \Phi_i^{\text{bulk}} \\ \Delta \Phi_m^{\text{bulk}} \\ \Delta c^{\text{SCL}} \\ \Delta \Phi_i^{\text{SCL}} \end{bmatrix}_{i+1} \\ & \times \\ & = \begin{bmatrix} \mathbf{R}_{\Phi_i}^{\text{bulk}} \\ \mathbf{R}_{\Phi_m}^{\text{bulk}} + \mathbf{R}_{\Phi_s}^{\text{SCL}} \mathbf{A} \\ \mathbf{R}_c^{\text{SCL}} \mathbf{A} \\ \mathbf{R}_{\Phi_i}^{\text{SCL}} \mathbf{A} \end{bmatrix}_{i+1}. \end{aligned} \quad [33]$$

Solution of the linearized system of equations.—Within this work, we choose a monolithic coupling scheme to solve the outlined linear system of equations where equations from the bulk domain and the SCL domain are coupled. As shown elsewhere (e.g. in Ref. 38 for n-field problems or in Ref. 39 for electrochemical problems), the monolithic solution approach is seen as superior considering robustness and often also with respect to efficiency compared to other schemes like partitioned coupling or sub-cycling for various types of applications. The most prominent drawback of the monolithic coupling approach is, that the underlying matrix is comparably ill-conditioned. This is caused by additional entries in the matrix that are far away from the main diagonal, and entries with different orders of magnitude originating from the different domains, dimensions, and discretization coarseness that are coupled. Thus, standard

Table I. Material parameters of LLTO, initial and boundary conditions, and natural constants for all simulations.

Quantity	Symbol	Value	Source
ionic conductivity	σ	$0.02 \frac{\text{S}}{\text{m}}$	Ref. 42
maximal concentration	c_{max}	$14\,214 \frac{\text{mol}}{\text{m}^3}$	calculated
bulk concentration	c_{bulk}	$9\,476 \frac{\text{mol}}{\text{m}^3}$	calculated
lower bound of bulk concentration	$c_{\text{bulk, min}} = 0.999 c_{\text{bulk}}$	$9\,466.5 \frac{\text{mol}}{\text{m}^3}$	defined
upper bound of bulk concentration	$c_{\text{bulk, max}} = 1.001 c_{\text{bulk}}$	$9\,485.5 \frac{\text{mol}}{\text{m}^3}$	defined
tolerance of concentration	c_{ϵ}	$10^{-4} \frac{\text{mol}}{\text{m}^3}$	defined
susceptibility in SCLs	χ	10^5	Ref. 43
difference in partial molar volume	$\Delta \nu = \nu_+ - \nu_-$	0	Ref. 35
transference number of cations	t_+	1	defined
charge number	z	1	Ref. 36
average molar mass	M	$0.168822 \frac{\text{kg}}{\text{mol}}$	calculated in Ref. 36
average mass density	ρ	$4\,000 \frac{\text{kg}}{\text{m}^3}$	Ref. 44
initial concentration	c_0	$9\,476 \frac{\text{mol}}{\text{m}^3}$	equals c_{bulk}
difference in potential	$\Delta \Phi$	2V	defined, as in Ref. 36
temperature	T	298K	defined, as in Ref. 36
dielectric permittivity of vacuum	ϵ_0	$8.85 \cdot 10^{-12} \frac{\text{F}}{\text{m}}$	defined, as in Ref. 36
Faraday constant	F	$9.65 \cdot 10^4 \frac{\text{C}}{\text{mol}}$	defined, as in Ref. 36
universal gas constant	R	$8.314 \frac{\text{J}}{\text{molK}}$	defined, as in Ref. 36

iterative solvers that are required to solve realistic microstructures with a large number of unknowns, are not applicable anymore and tailored preconditioners are required. We choose a combined Block-Gauß-Seidel and Algebraic-Multigrid preconditioner as outlined in Ref. 40. The core idea is to split the full linear system of equations into subblocks, that are physically meaningful, e.g. geometric domains or types of primary variables, and apply a Block-Gauß-Seidel scheme on these blocks. This already improves the condition of the subblocks compared to the full system of equations. Additionally, we perform a prescaling of the rows and the columns of the subblocks to further improve the condition of the subblocks. Finally, we apply an Algebraic-Multigrid preconditioner to the subblocks on the main diagonal within the Block-Gauß-Seidel iteration.

Results

The results presented in this Section are computed with BACI,⁴¹ our in-house multi-physics research code. We begin with approximating an optimal length and discretization size for the SCL domain, validating the proposed model, and conclude with showing the applicability of the model to realistic microstructures.

Materials.—The idea of this paper is not to investigate the behavior of the SCL for different materials and conditions. Instead, we want to analyze the proposed model in more detail. Hence, we restrict ourselves to one set of material parameters (for lithium lanthanum titanate - LLTO) throughout this work if not explicitly stated to be different. All relevant material parameters, initial conditions, and physical constants are chosen as in Ref. 36 and are listed in Table I.

Two characteristic values to quantify an SCL.—We compute two characteristic quantities to quantify SCLs: the spatial thickness $d_{\text{SCL}}(\mathbf{x})$ and the integrated free charge Q_{SCL} . By using fixed values for $c_{\text{bulk,min}}$ and $c_{\text{bulk,max}}$ we can define the thickness of the SCL by

$$d_{\text{SCL}}(\mathbf{x}) = \xi(\mathbf{x}) \text{ where } \begin{cases} \text{argmin}(c(\xi(\mathbf{x})) > c_{\text{bulk,min}}) & \text{if } c < c_{\text{bulk}} \\ \text{argmin}(c(\xi(\mathbf{x})) < c_{\text{bulk,max}}) & \text{else} \end{cases} \quad [34]$$

The integrated deviation from the neutrally charged state Q_{SCL} is computed as the integrated difference of the concentration c from the bulk concentration c_{bulk} scaled by the charge number z and Faraday's constant F to obtain a charge

$$Q_{\text{SCL}} = zF \int_{\Omega_{\text{SCL}}} (c(\mathbf{x}) - c_{\text{bulk}}) d\Omega, \quad [35]$$

where Ω_{SCL} can be divided into the part at the anode $\Omega_{\text{SCL,a}}$ and at the cathode $\Omega_{\text{SCL,c}}$, and subsequently the integrated values $Q_{\text{SCL,a}}$ and $Q_{\text{SCL,c}}$, respectively. From the conservation of mass and charge we know, that a consistent formulation needs to fulfill $Q_{\text{SCL,a}} + Q_{\text{SCL,c}} = Q_{\text{SCL}} = 0 \forall t$.

Suitable representation of the SCL domain.—We estimate the optimal length and discretization size for the SCL domain within the coupled model based on simulations with a one-dimensional model as outlined before and the parameters from Table I.

Optimal length of the SCL domain.—While the geometric representation of the bulk domain Ω_{bulk} is already defined by the problem statement, the extension l_{SCL} of the SCL domain Ω_{SCL} has to be determined for the proposed coupling approach. We select it based on the following two criteria to minimize the approximation errors defined before:

1. The length of the SCL domain l_{SCL} must be large enough to enable the complete formation of SCLs at interfaces of the electrodes with the solid electrolyte $\Gamma_{\text{SCL-bulk}}$. This can be expressed in the requirement of vanishing gradients of the concentration $\nabla c(\xi = l_{\text{SCL}}) = 0 \forall t$ in Ω_{SCL} in accordance with Eq. 9.
 2. The length of the SCL domain l_{SCL} must be as small as possible to minimize the geometric error and the compatibility error. We combine two findings established in the literature to estimate a value of l_{SCL} :
1. The ratio $\frac{l_{\text{SCL}}}{l_{\text{SE}}}$ is proportional to a non-dimensional length scale λ , which is similar to the Debye-length of double layers in liquid electrolytes³⁵ and defined as

$$\lambda = \sqrt{\frac{k_{\text{B}} T \epsilon M}{e_0^2 l_{\text{SE}}^2 \rho}}, \quad [36]$$

with Boltzmann constant k_{B} , elementary charge e_0 , molar mass M , and mass density ρ . Smaller values of λ correspond to thinner SCLs if identical boundary conditions are applied.¹⁸ From this parameter, we deduce, that $l_{\text{SCL}} \propto \sqrt{T}$.

2. At the low-temperature limit, i.e. $T \rightarrow 0\text{K}$, the spatial extensions $l_{\text{SCL,c}}$ and $l_{\text{SCL,a}}$ of one-dimensional SCLs can be expressed analytically³⁶ as

$$l_{\text{SCL,c}} = \sqrt{\frac{2\epsilon \Delta\Phi}{F} \frac{z_- c_-}{(z_+ c_{\text{max}} + z_- c_-)(z_- c_-)}}, \quad [37]$$

$$l_{\text{SCL,a}} = -\frac{z_-}{\frac{c_{\text{max}}}{z_+} + z_-} l_{\text{c}} = f_{\text{sym}} \cdot l_{\text{c}}. \quad [38]$$

Both, $l_{\text{SCL,c}}$ and $l_{\text{SCL,a}}$ are proportional to the square root of the applied difference in electric potential $l_{\text{SCL,c}}, l_{\text{SCL,a}} \propto \sqrt{\Delta\Phi}$. Depending on the ratio $\frac{c_-}{c_{\text{max}}}$, the respective lengths can significantly differ. Therefore, we introduce a symmetry factor f_{sym} to quantitatively capture this asymmetry. For the material parameters used in this work, the symmetry factor is computed as $f_{\text{sym}} = \frac{3}{2}$, such that $l_{\text{SCL,a}} > l_{\text{SCL,c}}$.

Now, we can estimate the length of the SCL by the following ansatz

$$l_{\text{SCL,c,a}}^*(\Delta\Phi, T) = (k_0 + k_1 \sqrt{T}) \cdot l_{\text{SCL,c,a}}, \quad [39]$$

with the unknown constants k_0 and k_1 . By performing one-dimensional simulations with different values for $\Delta\Phi$, T , and blocking electrode conditions, we can compute k_0 and k_1 . Additionally, we introduce a safety factor ζ to cover the impact of complex three-dimensional microstructures which cannot be considered in this estimate and define

$$l_{\text{SCL}} = \zeta \cdot \max\{l_{\text{c}}^*, l_{\text{a}}^*\}. \quad [40]$$

For the aforementioned material parameters, and a safety factor of $\zeta = 2$ we get $l_{\text{SCL}} = 0.4\mu\text{m}$. We use this value throughout the remainder of this work.

We verify our choice of l_{SCL} by considering an extreme case where the entire difference in electric potential occurs inside one SCL. Therefore, the conditions for blocking electrodes are applied, and additionally, the concentration is fixed on one side of the domain $c(\xi = l_{\text{SCL}}) = c_{\text{bulk}}$ to obtain a single-sided SCL. The result for this setup is shown in Fig. 4a. It can be seen, that the gradients of the concentration vanish for $\xi > 0.2\mu\text{m}$, such that $l_{\text{SCL}} = 0.4\mu\text{m}$ is a sufficiently large choice. This estimated size is in good agreement with measurements, e.g. $d_{\text{SCL}} = [0.2; 0.3]\mu\text{m}$.¹⁷

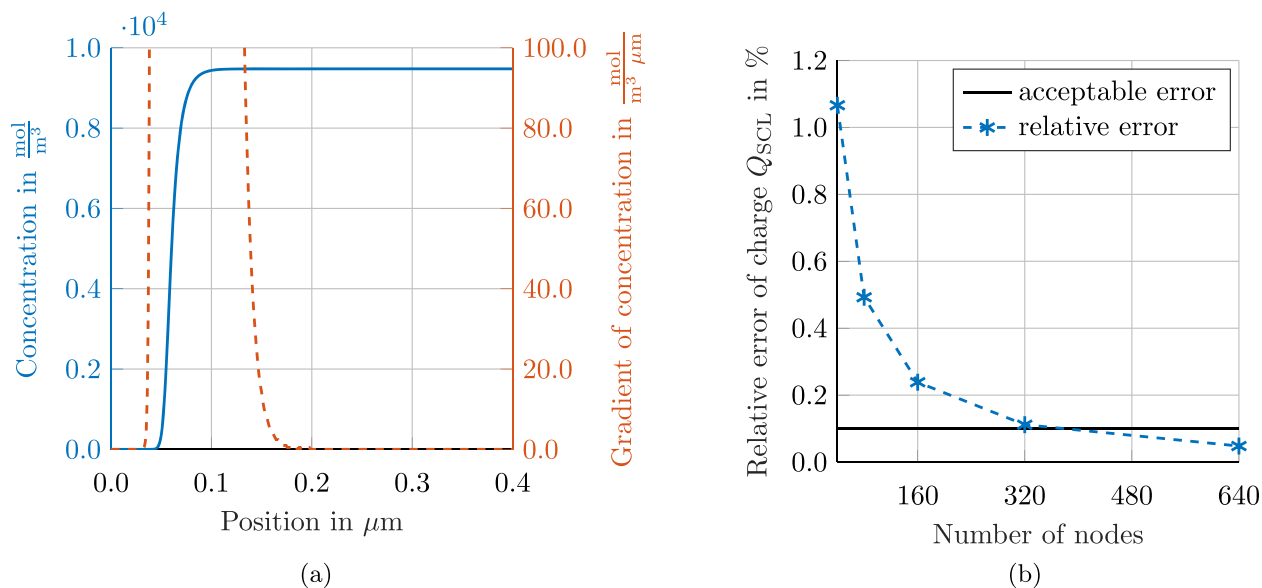


Figure 4. Determining the optimal length and discretization size for the SCL domain. (a) Concentration and gradient of the concentration show that $l_{\text{SCL}} = 0.4 \mu\text{m}$ is a good choice for the length of the SCL domain for the used material parameters and boundary conditions. (b) Relative error of integrated charge Q_{SCL} in the steady state for the used material parameters and boundary conditions.

Optimal discretization size of the SCL domain.—While the length of the SCL domain is obtained based on the maximal expected size of the SCL, the discretization size is determined by the minimal expected size of the SCL to resolve the change in gradients there. Thus, we perform a spatial convergence analysis by comparing the stored charge Q_{SCL} inside the smaller SCL for different sizes of the discretization. We conduct the simulation for $n_{\text{ele}} = \{40, 80, 160, 320\}$ and choose $n_{\text{ele}} = 2560$ as the reference solution. Thus, the reference discretization has four times the nodes of the finest discretization in the convergence study. Again, we investigate a single-sided SCL. Figure 4b illustrates that for the used material parameters and boundary conditions approximately 300 nodes are required to obtain a relative error below 0.1% which is considered as very small. We emphasize, that the required number of nodes per l_{SCL} is a function of the symmetry factor f_{sym} . In general, higher values of f_{sym} increase the computational effort, as it leads to a larger length l_{SCL} and requires a finer discretization.

Validation of the outlined model.—Different strategies are followed to validate the outlined model: Solving a pseudo one-dimensional problem, testing for conservation properties, and comparing the results with those obtained by a fully resolved model.

Validation of the coupled three-dimensional model as pseudo one-dimensional model.—We compare the results of our coupled model that combines one- and three-dimensional discretizations (“coupled SCL model”) with the result of a pure one-dimensional model as shown before (“pure SCL model”). For comparison, the x-dimension of the coupled approach matches exactly the length of the pure one-dimensional model $l_{\text{coup}} = l_{\text{1D}}$. The length of the coupled problem is $l_{\text{coup}} = 2l_{\text{coup,SCL}} + l_{\text{coup,bulk}}$ (see Fig. 5). The other two dimensions in the coupled SCL model are chosen such that a reasonable aspect ratio of the three-dimensional domain is maintained. The three-dimensional domain of the coupled SCL model is discretized using two equal-sized hexahedral elements with linear shape functions, while the one-dimensional domain of the coupled SCL model consists of 2400 line elements with linear shape functions, meaning 300 nodes in each SCL discretization. The pure SCL model is discretized with 1800 line elements, such that the discretization inside the SCL domain is identical for both models.

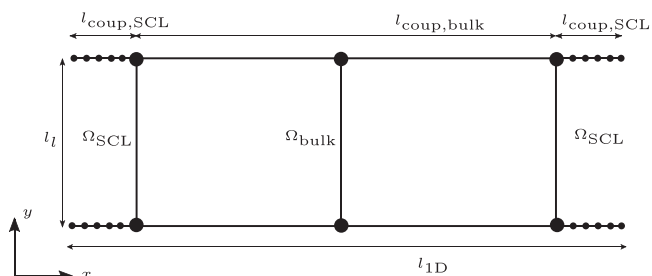


Figure 5. Schematic sketch of the computational domain for comparison of the coupled three-dimensional model and the one-dimensional model.

We prescribe a scenario with blocking electrodes: A difference in potential $\Delta\Phi$ is applied to both ends of the domain, while the flux of mass outside of the considered domain is prohibited. All relevant parameters are summarized in Table II. In Fig. 6a we compare the results of the concentration and in Fig. 6b the electric potential from the pure SCL model with the results from the coupled SCL model for different points in time.

The results computed with the two models are in very good agreement. Even in regions where the curvature of both the concentration and the electric potential, changes most (see zooms) the deviation is negligible.

Analyzing the results of the pure one-dimensional model allows quantifying the approximation error labeled as “model error”. In Fig. 7, it can be seen that the concentration inside the bulk domain is very close to the bulk concentration c_{bulk} throughout the entire simulation time. This shows that the only assumption in the derivation for the equations of the bulk domain, namely that the concentration remains at the fixed value c_{bulk} , is justified.

Besides, we want to quantify the approximation error, which we labeled “geometric error” by modifying the dimensions of Ω_{bulk} . As shown in Fig. 6b, most of the potential drop occurs inside the SCLs except for the first instances of time. This already shows that the influence of a slightly larger domain has a negligible influence on the global shape of the potential and the concentration. To investigate this in more detail, we choose $l_{\text{coup,bulk}} = l_{\text{1D}}$ and keep the size of the SCL domain untouched, such that $l_{\text{coup}} > l_{\text{1D}}$. In Fig. 8 we compare the results of the matching geometric size with the results of the

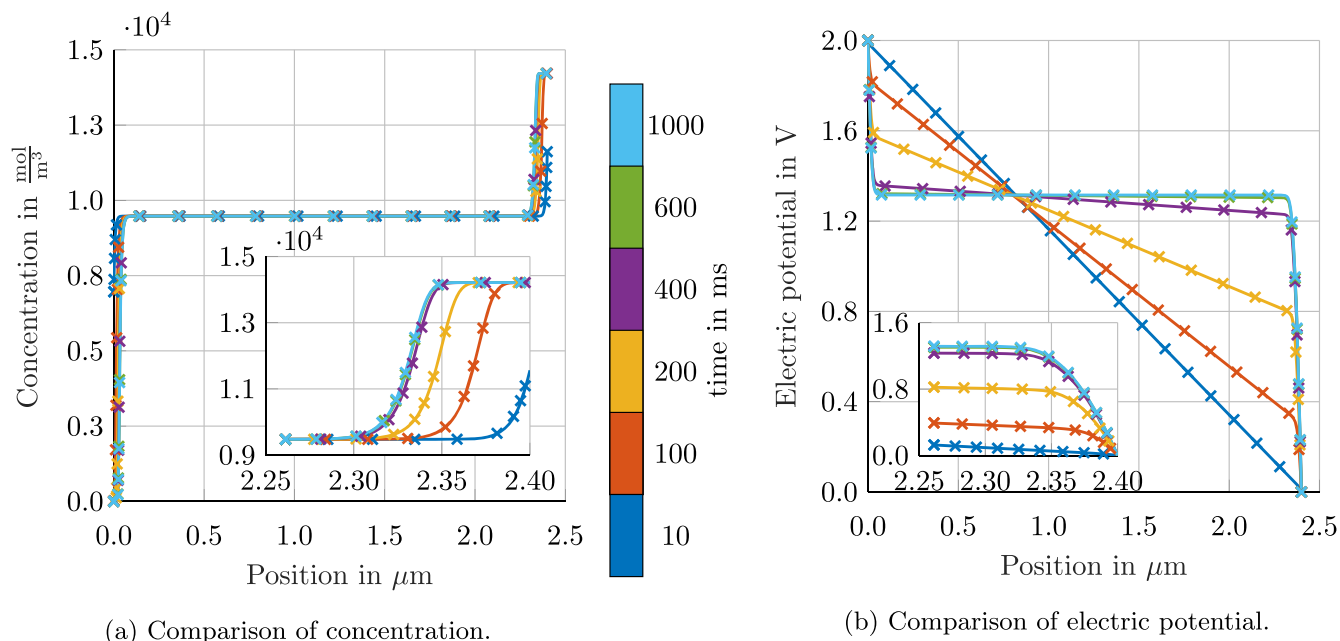


Figure 6. Comparison of concentration and electric potential for the pure SCL model (crosses) and the coupled SCL model (solid lines). The different time steps are assigned to the lines by color codes. The small figures inside the plots represent zooms into the SCL domains at the right side with a finer resolution of the crosses. Note, that the crosses do not represent the spatial discretization.

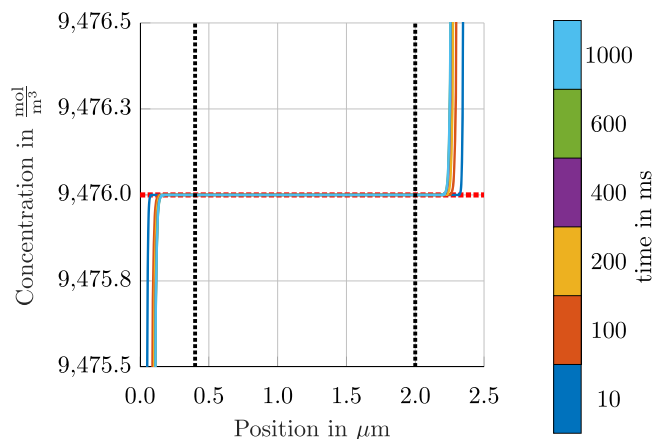


Figure 7. Zoom to concentration in the bulk domain computed with the pure one-dimensional model at different time steps approximately equals the bulk concentration (red line) inside the bulk domain. The vertical lines separate the bulk domain from the SCL domain.

Table II. Parameters for comparing results between pure and coupled three-dimensional Space-Charge-Layer model.

Quantity	Symbol	Value
length of domain	$l_{\text{coup}} = l_D$	2.4 μm
lateral length	l_l	0.4 μm
length of SCL domain	$l_{\text{coup,SCL}}$	0.4 μm
coupled: number of elements (SCL)	$n_{\text{ele,SCL}}$	2 400
coupled: number of elements (bulk)	$n_{\text{ele,bulk}}$	2
pure: number of elements	$n_{\text{ele,1D}}$	1 800
time step size	Δt	1 ms
total time	t_{max}	1 s

enlarged geometry by zooming into the plot of the concentration (Fig. 8a) and the electric potential (Fig. 8b) at the SCL on the left side of the domain.

As expected, we introduce an error in the shape of the electric potential that decreases toward the steady state, while the error in the concentration in the bulk is negligible. However, in this academic example, we triggered the geometric error on purpose to show its influence but want to emphasize, that here $l_{\text{SCL}} \ll l_{\text{SE}}$ is not valid anymore.

Validation of conservation properties.—For the validation of conservation properties, we use a geometry, that is not pseudo-one-dimensional but still as simple as possible (see Fig. 9). It consists of one spherical particle embedded in the bulk solid electrolyte representing the cathode (e.g. NMC). The anode is represented by a planar surface (e.g. lithium metal). The size of the geometry is reduced by making use of symmetry. All relevant parameters are listed in Table III. Again, we apply a difference in potential $\Delta\Phi$ without any flux of mass between both electrodes to represent the steady state is reached. For visualization, we take snapshots at $t = \{0, 0.31, 0.625, 1.25, 2.5, 10.0\}$ s to present the three-dimensionally resolved development of the electric potential and of the thickness of the SCL at $\Gamma_{\text{SCL,c}}$ over time (see Fig. 10).

It is clearly visible, that the thickness of the SCL changes over time and also significantly varies at different spatial positions. As expected, the electric potential converges toward a constant value in the steady state and thus, also the thickness converges toward a constant value as the thickness is determined by the difference in potential across the SCL.

We expect the integrated deviation of charge from the neutrally charged state as defined before to remain constant over time due to the conservation of mass. For visualization, we split this integral into one part at the anode $Q_{\text{SCL,a}}$ and one part at the cathode $Q_{\text{SCL,c}}$. In Fig. 11a we show the development of Q_{SCL} , $Q_{\text{SCL,a}}$, and $Q_{\text{SCL,c}}$ over time.

We can clearly see that $Q_{\text{SCL,a}}$ increases, while $Q_{\text{SCL,c}}$ decreases over time, but their sum remains - in the expected bounds of the

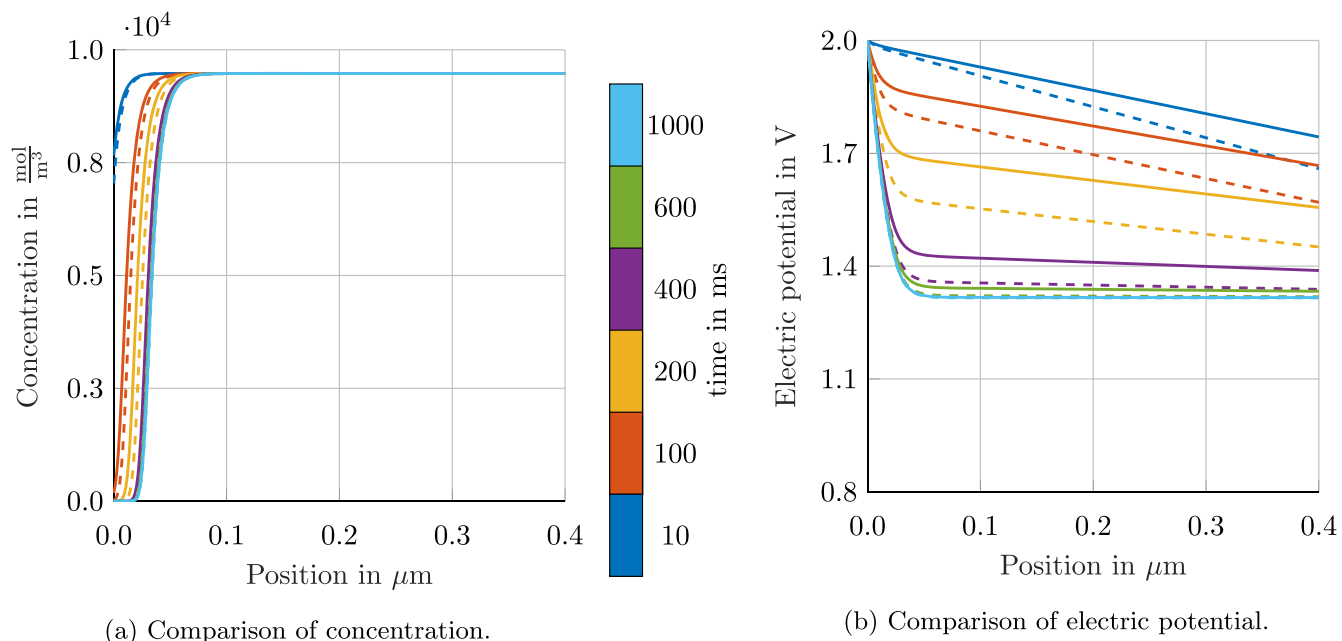


Figure 8. Comparison of concentration and electric potential for the matching geometry (dashed lines) and the enlarged geometry (solid lines). The different time steps are assigned to the lines by color codes.

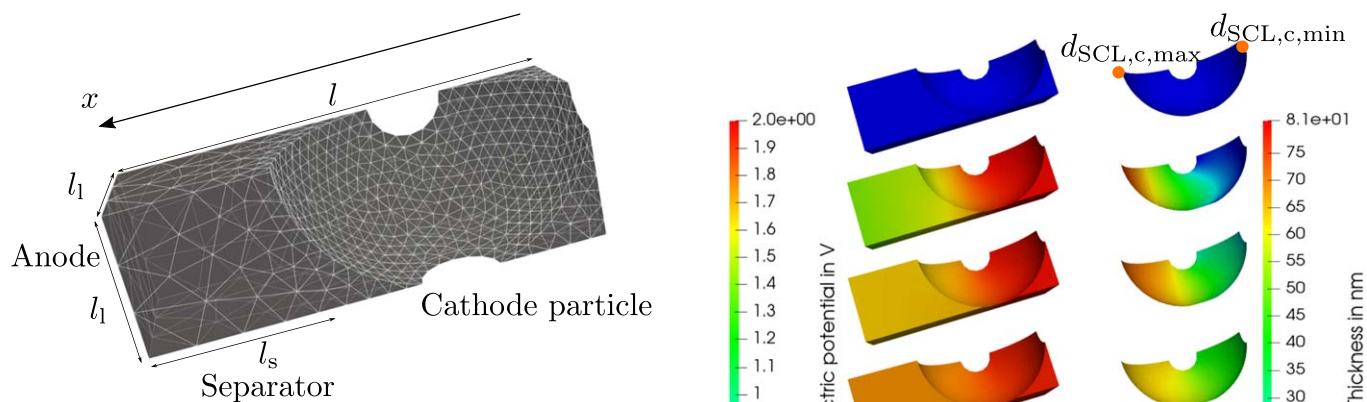


Figure 9. Geometric representation of the geometry for validation of conservation properties.

Table III. Parameters for testing conservation properties.

Quantity	Symbol	Value
length of domain	l	$3 \mu\text{m}$
diameter of sphere	d	$2 \mu\text{m}$
lateral length	l_1	$0.97 \mu\text{m}$
length separator	l_s	$1 \mu\text{m}$
length of SCL domain	$l_{\text{coup,SCL}}$	$0.4 \mu\text{m}$
number of nodes bulk	n_{bulk}	2 384
number of nodes SCL	n_{SCL}	103 500
time step size	Δt	5 ms
total time	t_{max}	10 s

numerical accuracy - constant. This shows that our formulation guarantees conservation properties.

From this geometrically simple example, we can derive further insights beyond the proof of conservation properties considering the development of the thickness of the SCL, which strongly differs

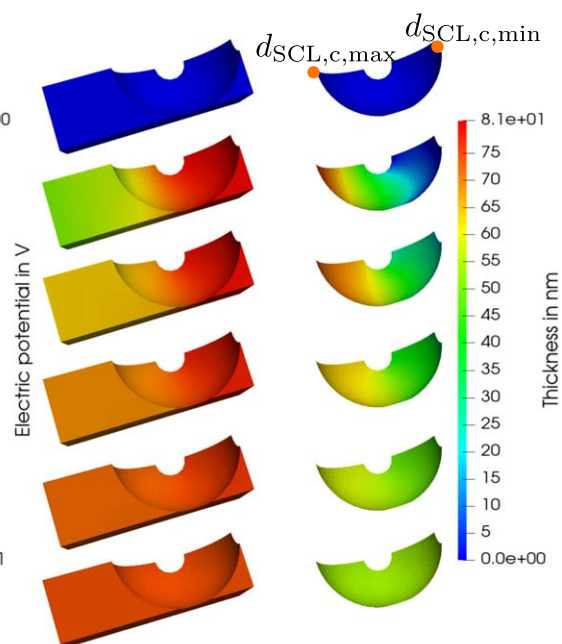


Figure 10. Temporal development of electric potential and thickness of SCL from the initial state to the steady state (top to bottom). The locations where the minimal and maximal thickness of the SCL occurs are highlighted with an orange dot.

depending on its local position. While the thickness of the SCL on $\Gamma_{\text{SCL-c}}$ close to the anode develops instantly, the SCL on the opposite side on $\Gamma_{\text{SCL-c}}$ develops much slower. In Fig. 11b we compare the minimal thickness $d_{\text{SCL,c,min}} = \min(d_{\text{SCL,c}})$ and the maximal thickness $d_{\text{SCL,c,max}} = \max(d_{\text{SCL,c,max}})$ of the SCL at the interface to the cathode. The minimal thickness converges monotonically toward the steady state, while the maximal thickness rapidly increases to a value, that is larger than the final value at the steady state and eventually decreases again toward the thickness at the steady state. This unintuitive behavior can be explained by investigating the impedance between both electrodes (see Fig. 10). The total

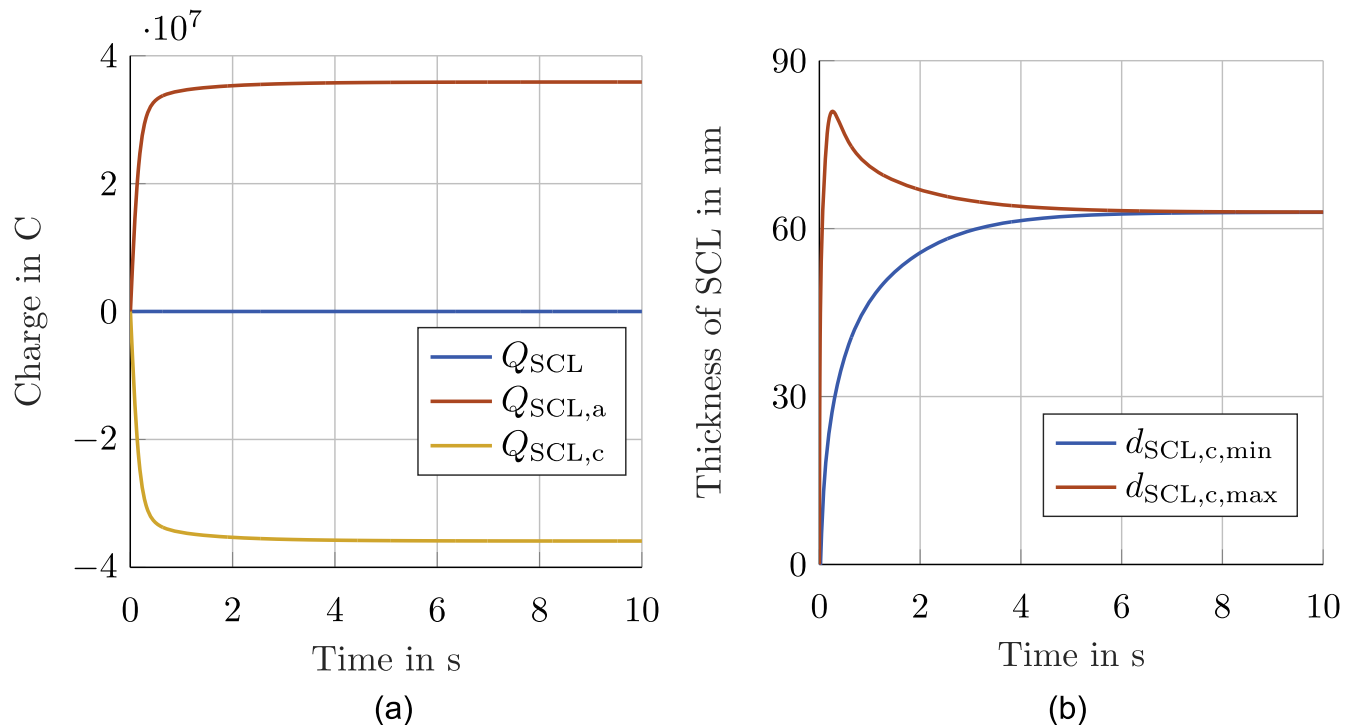


Figure 11. Results for the validation of conservation properties. (a) Temporal development of the integrated deviation of the charge from the charge-neutral state for the SCL at the anode, at the cathode, and their sum. (b) Temporal development of minimal and maximal thickness of SCLs at the spherical electrode.

impedance is composed of the sum of the impedance in the bulk and in the SCL and its minimal value defines the favored conduction path. The impedance in the bulk electrolyte scales with the length through the electrolyte. The impedance in the SCL increases with increased stored charge. During the transient phase, the minimal total impedance continuously changes, as the impedance from the SCL changes due to more stored charge. Thus, the favored conduction path changes to regions with more contributions from the impedance of the bulk. This can be observed in the electric potential inside the bulk electrolyte which at the beginning features a gradient only between the anode and regions on $\Gamma_{SCL,c}$ closest to the anode. Later, the gradient is visible inside the entire bulk domain, before it vanishes completely in the steady state.

Additionally, we observe in the steady state that the electric potential in the bulk domain differs from the electric potential in the pseudo one-dimensional case computed in the examples before. This is caused by the different areas of the interfaces with the anode and the cathode, respectively. As shown before, the total charge within both SCLs sum up to zero, but due to the different interface areas, the local charge density is different, and thus, the entire shape of the SCL. Again, this highlights the necessity to three-dimensionally resolve SCLs.

Comparison of the solution without simplification assumptions.—

For further validation of the proposed model, we compare the solution computed with the proposed model with the solution computed with a model without further assumptions, i.e. solving the non-reduced equations in all three dimensions of space. The geometry for both models is shown in Fig. 12 and the respective parameters are summarized in Table IV. The geometric dimensions are chosen such that the domain of the coupled model including both the bulk domain and the SCL domain equals the domain of the model without assumptions. The electrode is represented by a cylinder. To reduce the computational effort of the models, we design the problem as two-dimensional, with constant thickness in the third dimension of space. Additionally, we set the concentration at the right boundary to c_{bulk} to obtain a single-sided SCL at the cylindrical electrode. Thus, we need a strong refinement of the mesh

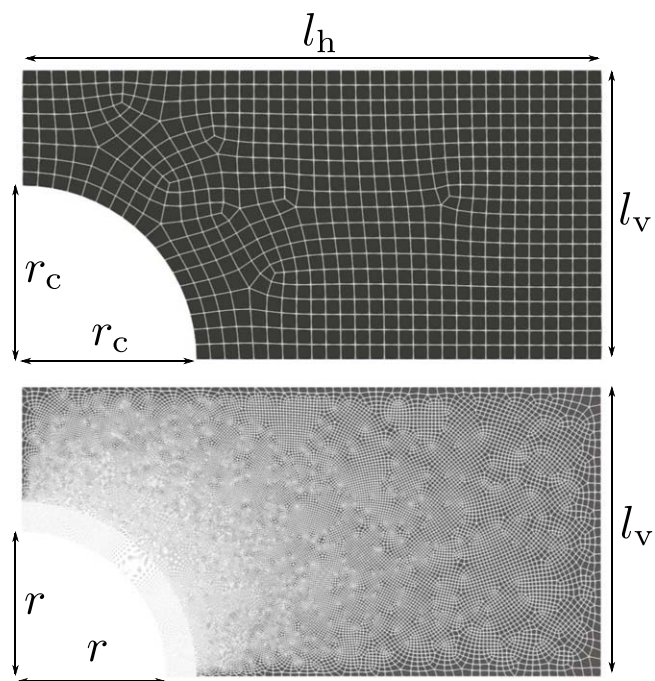
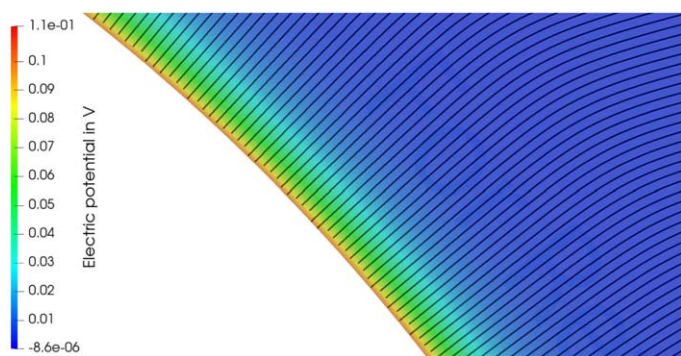


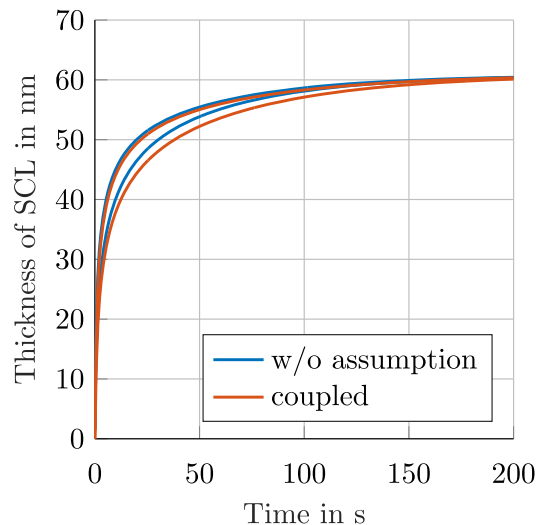
Figure 12. Geometric representation of the coupled model (top) and the model without assumptions (bottom).

only at the cylindrical electrode. In contrast to the examples before, we choose the difference in electric potential to $\Delta\Phi = 0.1V$ to reduce the size of the SCL, which is evaluated according to Eq. 40 to $l_{SCL} \approx 0.1\mu m$. The difference in electric potential is applied between the cylindrical electrode and the right boundary.

First, we want to justify the assumption, that the main effects inside the SCL are one-dimensional and thus estimate the compatibility error. Therefore, we visualize the gradient of the electric potential computed



(a)



(b)

Figure 13. Results to quantify the compatibility error. (a) Electric potential (color bar) and gradient of electric potential (streamlines) in the region of the SCL in the steady state. (b) Temporal development of the maximal and minimal thickness of the SCL computed with the model without assumptions (blue) and the coupled model (red).

Table IV. Parameters for comparison of the coupled model and the model without assumptions.

Quantity	Symbol	Value
radius of cylinder	r	$0.5 \mu\text{m}$
radius of cylinder (coupled)	r_c	$0.6 \mu\text{m}$
vertical edge length	l_v	$1 \mu\text{m}$
horizontal edge length	l_h	$2 \mu\text{m}$
length of SCL domain (coupled)	l_{SCL}	$0.1 \mu\text{m}$
number of nodes	n	150 650
number of nodes (coupled, total)	n_c	13 136
time step size	Δt	0.2 s
total time	t_{max}	200 s

with the model without assumptions (see Fig. 13a). It can be seen that the gradient at the interface to the electrode is perfectly perpendicular as expected. With increasing distance to the electrode, the direction of the gradient begins to deviate from the perpendicular direction. This means that the assumption, that the effects inside the SCL are mainly one-dimensional is sufficiently satisfied, as long as the domain Ω_{SCL} is small enough.

By comparing the temporal development of the minimal and maximal thickness of the SCL between the model without assumptions and the coupled model, we observe a good agreement. As expected, the deviation of the minimal thickness is larger compared to the maximal thickness. The minimal thickness occurs at the left-most point on the cylindrical electrode where the normal vector is perpendicular to the main direction of the gradient of the electric potential inside the bulk domain, as cations cannot redistribute tangentially within the SCL. Instead, they need to travel through the bulk domain in order to move tangentially to the surface before entering another SCL domain. Therefore, the redistribution paths are longer compared to those in the fully resolved model. Thus, the compatibility error is more prominent during the equilibration process than in the steady state. There, nearly perfect alignment of d_{SCL} can be observed between both models, as all tangential redistribution is accomplished.

This model allows not just the comparison of physically meaningful quantities but also to compare the differences in computational efficiency. While the CPU time of the model without

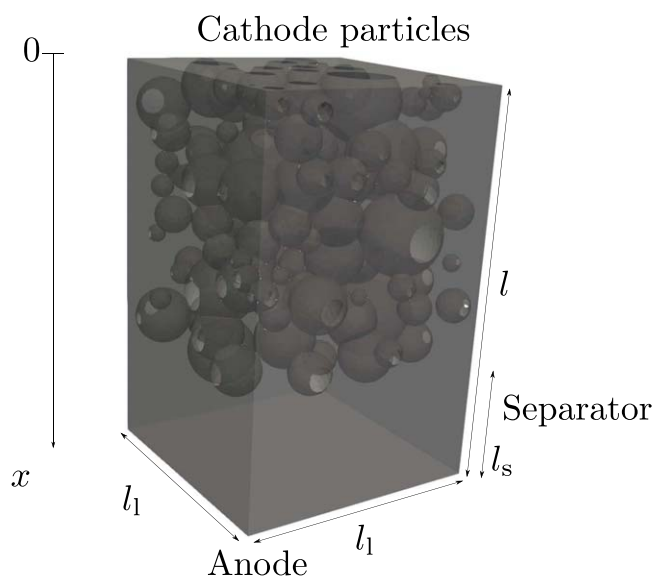
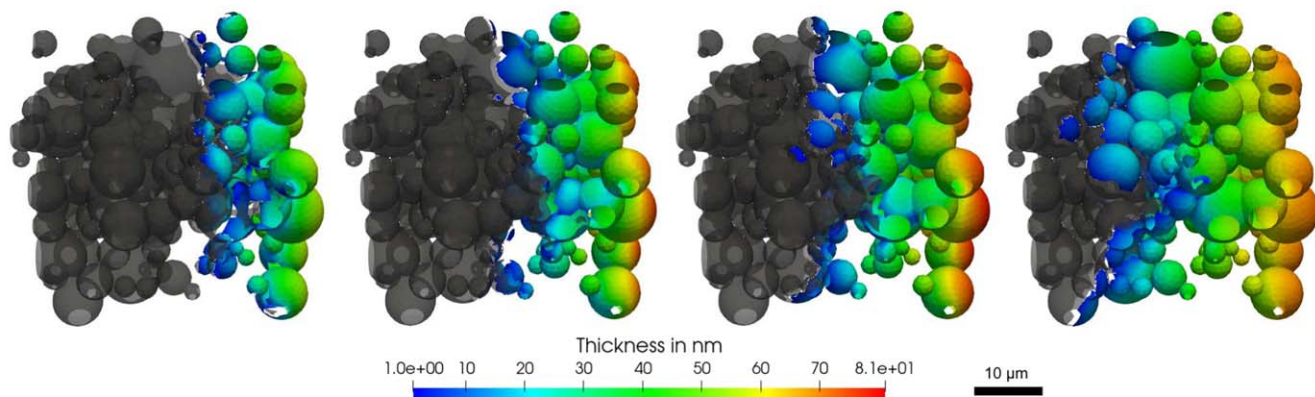


Figure 14. Dimensions of the realistic geometry.

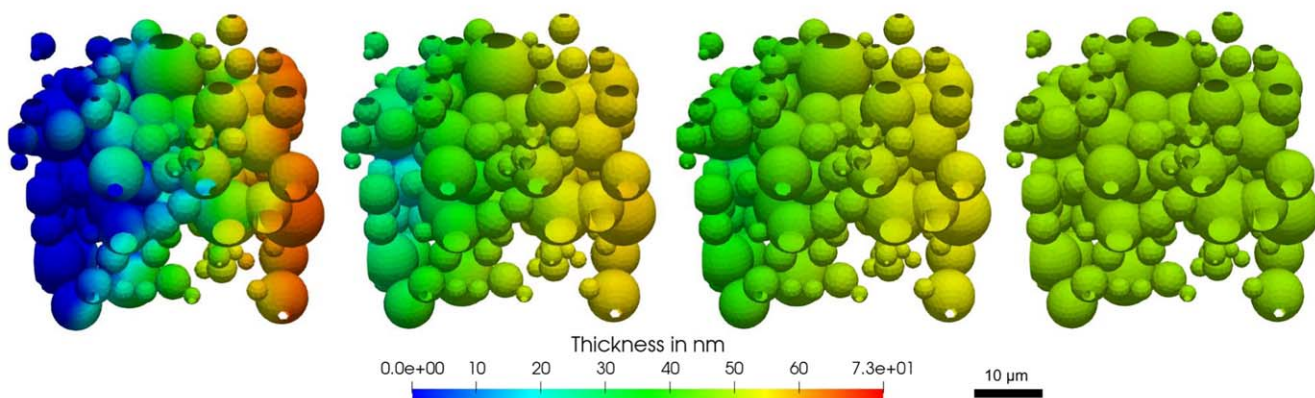
assumptions was in the order of days, the coupled model was solved within minutes.

Numerical experiment using a realistic microstructure.—Beyond the academic examples we showed before to validate the proposed approach, we want to apply the model to a geometrically realistic microstructure to show its capabilities.

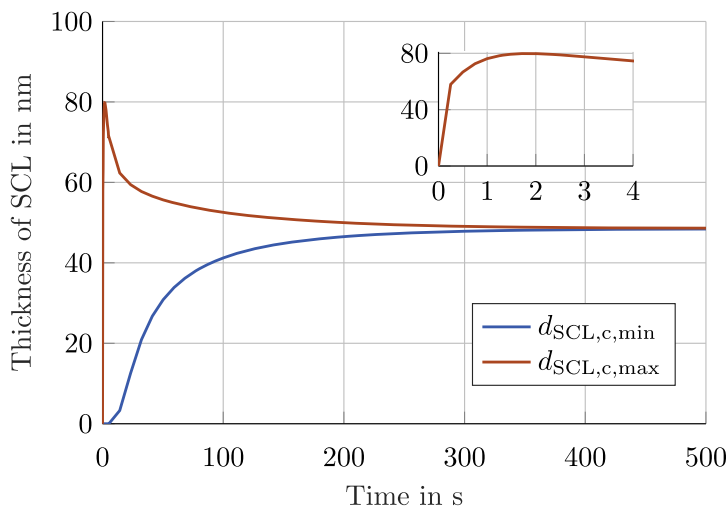
Geometric representation and spatial discretization.—We create the geometric representation of the realistic microstructure using a setup, where perfectly shaped spherical particles as the active material of the cathode (e.g. NMC particles), and a planar foil as the anode (e.g. lithium metal) are assumed (see Fig. 14 and Table V). For this purpose we employed the following workflow: The domain of the solid electrolyte is split into the separator $\Omega_{\text{bulk, s}}$ and the part of the solid electrolyte inside the composite cathode $\Omega_{\text{bulk, CC}}$. Both domains have the same lateral length l_1 , while their axial length l_s , and $l_{\text{CC}} = l - l_s$ differs. The diameter of the cathode particles



(a)



(b)



(c)

Figure 15. Temporal development of the thickness of the SCL at the cathode. (a) Propagation of the thickness of the SCL through the geometrically resolved microstructure at the beginning of the formation process at $t = \{0.25, 1, 2, 5\}$ s. (b) Equalization of the SCL thickness towards the steady state at $t = \{8.25, 35.25, 65.25, 491.25\}$ s. (c) Temporal development of maximal and minimal thickness of SCL. The subfigure represents a zoom into the interval $t = [0; 4]$ s.

follows a log-normal distribution with mean μ and variance σ^2 . We create as many particles following the log-normal distribution as needed to satisfy a given volumetric ratio r of the active material and the solid electrolyte. The position of the center points of the particles is computed using a simulation with the discrete element method to obtain a spatially realistic distribution of the particles. Consequently, the SCL domain is defined on that surface $\Omega_{\text{SCL}} = \Gamma_{\text{SCL-bulk}} \times l_{\text{SCL}}$.

The interface of the solid electrolyte and the cathode is on the surface of the spheres, and the interface of the solid electrolyte and the anode is the planar surface at the bottom of Fig. 14. We discretize the geometry using tetrahedral elements with the meshing tool *Coreform Cubit 2021.3*. The interface nodes of the bulk solid electrolyte domain and of the electrode domain are connected with line elements representing the SCL domain.

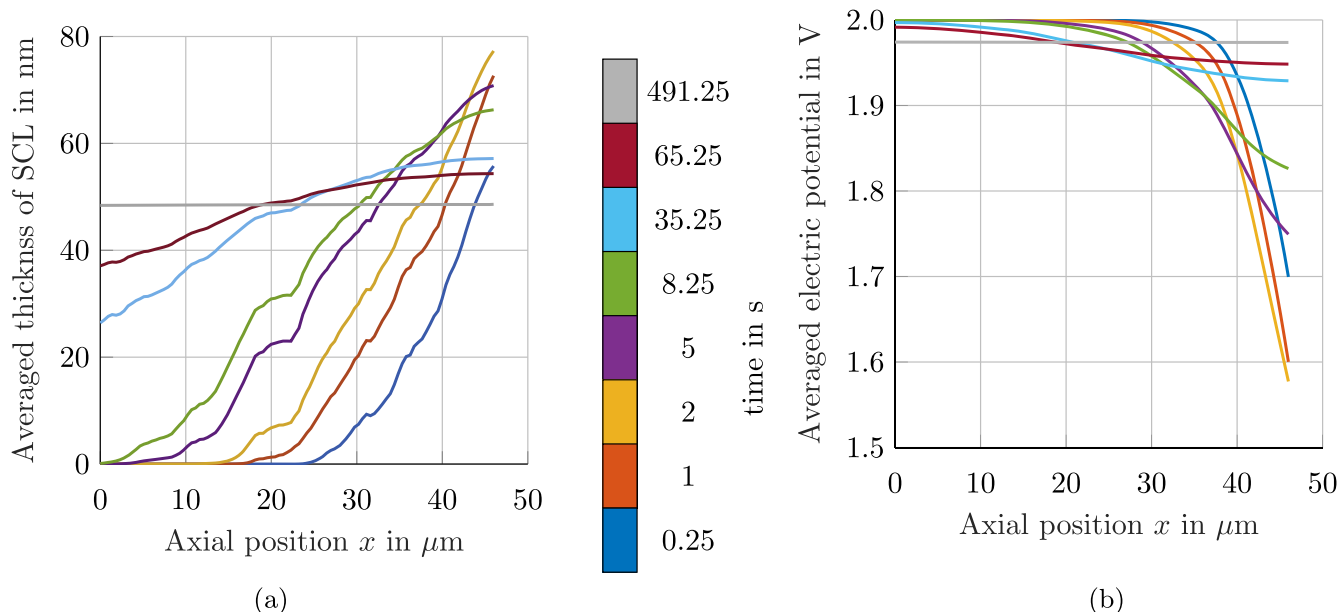


Figure 16. Laterally averaged quantities. (a) Temporal development of the laterally averaged thickness of the SCL along the axial coordinate x . (b) Temporal development of the laterally averaged potential of the solid electrolyte along the axial coordinate x .

Table V. Parameters for the simulation of the realistic geometry.

Quantity	Symbol	Value
length of domain	l	$70 \mu\text{m}$
length of solid electrolyte separator	l_s	$17 \mu\text{m}$
lateral length	l_l	$45 \mu\text{m}$
log-normal distribution of diameter of cathode particles	μ	1.8189
	σ	0.4589
volumetric ratio of AM and SE in composite cathode	r	0.502
length of SCL domain	l_{SCL}	$0.15 \mu\text{m}$
number of nodes in bulk domain	n_{bulk}	130 211
number of nodes in SCL domain	n_{SCL}	5 998 200
size of time step	Δt	$\begin{cases} 50 \text{ ms} & \text{if } t < 5 \text{ s} \\ 300 \text{ ms} & \text{else} \end{cases}$
total time	t_{max}	500 s

Results.—A difference in electric potential between both electrodes is applied. We set the electric potential at the anode to $\Phi_a = 0\text{V}$ and at the cathode to $\Phi_c = 2\text{V}$. Again, we want to study the transient behavior until the steady state is reached, such that we choose a total simulation time of 500 s.

At first, we analyze the thickness of the SCL d_{SCL} by plotting it in the three-dimensional geometric representation (see Fig. 15a) during its initial development at $t = \{0.25, 1, 2, 5\}$ s. For visualization, we disable the colorful representation if the thickness is below a threshold $d_{\text{SCL}}(x) < 1\text{nm}$ and otherwise assign a linear color bar to the thickness. This representation indicates the non-uniformness of the development of the thickness of the SCL: The dominating trend is comparable to the simplified examples we showed before, namely a propagation through the composite cathode beginning at the points closest to the anode. Due to the geometric complexity of the resolved microstructure, also an inhomogeneous behavior in the lateral plane is observable, which we want to discuss in more detail. The inhomogeneity can be explained by optimal percolation paths. The percolation path in the bulk is now not just defined by the theoretically shortest distance to the anode, but also by geometric obstacles increasing the percolation path, namely the active material particles. Obviously, these obstacles differ in the lateral plane and thus, explain the lateral inhomogeneity of Φ_{SCL} . We observe that the

SCL has already further developed where only very few active material particles are on the percolation path.

After an SCL has developed everywhere, a convergence toward an equal-sized thickness is observable. Again, we identify some areas close to the anode where a decrease in thickness occurs, such that the largest thickness is not present in the steady state, but after some instances of time. Figure 15b shows the thickness of the SCL at $t = \{8.25, 35.25, 65.25, 491.25\}$ s.

The observed inhomogeneous development of the thickness of the SCL can further be expressed in terms of maximal and minimal thicknesses $d_{\text{SCL},c,\text{min}} = \min(d_{\text{SCL},c})$ and $d_{\text{SCL},c,\text{max}} = \max(d_{\text{SCL},c})$, respectively (see Fig. 15c). While the maximal value of the thickness is reached within the first instances of time, the SCL at other positions has not yet developed at all.

As the dominating trend of all quantities is one-dimensional, we define laterally averaged quantities as

$$\bar{\Psi}(x) = \frac{\int_y \int_z \Psi(x, y, z) dz dy}{\int_y \int_z dz dy}. \quad [41]$$

In Fig. 16a we show the development of the laterally averaged thickness of the SCL at the cathode $\bar{d}_{\text{SCL}}(x)$ as a function of the axial

position x . At $x = x_{\max}$ the anode is nearest, while at $x = 0$ the distance to the anode is greatest. The different lines represent different points in time. Again, we see, the thickness developing through the solid electrolyte and converging toward a constant value at the steady state. Additionally, we observe the influence of the heterogenous geometry by the kink and almost horizontal line at $x \approx 20\mu\text{m}$. We would expect a smooth slope of the averaged thickness if the lateral dimensions would converge toward infinity. However, due to the finite length of the lateral dimension, the lateral planes geometrically differ from each other in a statistical sense and geometric inhomogeneities become visible. This is in good agreement with the observations in Fig. 15a, where an elongated percolation path is visible at the same location where the slope has the prominent kink in Fig. 16a.

Finally, we want to investigate the influence of the SCL on the bulk domain of the solid electrolyte by analyzing the laterally averaged electric potential $\bar{\Phi}(x)$ and plotting it over the axial direction (see Fig. 16b). The lines depict different points in time. At the beginning of the formation of the SCLs, we see that there is only a gradient in electric potential in regions close to $x = x_{\max}$, such that only there a development of the SCL is present. During the transient development, the SCL in the vicinity of $x = x_{\max}$ is nearly fully charged, such that the optimal percolation paths change toward regions at $x = 0$ until the electric potential has converged to a constant value in the steady state. Again, the electric potential is different from the potential computed in the examples before due to different interface areas at the anode and at the cathode side, as already discussed before.

Conclusions

We propose a novel approach to incorporate the effect of SCLs spatially resolved into a continuum model for all-solid-state batteries. To our knowledge, this is the first work reporting an approach to model the formation of SCLs in geometrically complex resolved microstructures by overcoming the computational limitations hindering the solution of fully resolved SCLs so far. The governing equations are already established in the literature^{35,36} and are thermodynamically consistently derived ensuring a positive production rate of entropy. Our approach is motivated by the dominating one-dimensional nature of SCLs as we have shown in this work. We divide the domain of the solid electrolyte into a domain that is close to the electrodes and the remaining domain. Inside the first domain, the partial differential equations are treated as one-dimensional while in the latter, we model them in three dimensions of space. This is advantageous, as a fine discretization, which is required in regions where SCLs develop, is now only required in one dimension of space. This significantly reduces the size of the used mesh and thus, enables a solution of the effects in SCLs even in complex and realistic cases. Furthermore, we assume that the cation concentration in the domain outside of the SCL region remains constant and subsequently simplify the equations inside this domain. Obviously, the proposed modeling approach introduces approximations into the system. We systematically determine, analyze, and quantify these approximations and show conservation properties of the model. Finally, we present the applicability of our model to realistic microstructures. Beyond the existing knowledge on the temporal development of SCLs in a one-dimensional setup, we observe a strong influence of the geometric inhomogeneity, like non-monotonic development of the thickness of the SCL or the inhomogeneous convergence of the electric potential toward the steady state.

The outlined model can in principle be applied to the case including mass transfer across the interface between electrode and electrolyte. However, a thermodynamically consistent model for the underlying kinetics is not yet known to the authors so far. Geometric variations like incorporating grain boundaries, as well as a systematic variation of the material parameters, are easily viable with the proposed model and should be the subject of future studies.

Funding

We gratefully acknowledge support by the Bavarian Ministry of Economic Affairs, Regional Development and Energy [project "Industrialisierbarkeit von Festkörperelektrolytzellen"] and the German Federal Ministry of Education and Research [project FestBatt 2 (03XP0435B)].

Appendix A. Summary of A Thermodynamically Consistent Model for Solid Electrolytes Including SCLs

We recall an approach to model solid electrolytes including SCLs as already derived in Refs. 35, 36 and define a consistent set of boundary and initial conditions.

Governing equations.—We will only summarize the underlying assumptions for the model of SCLs and summarize the resulting equations. For a more thorough derivation, we refer to recent work.³⁶

For the derivations of the set of equations, the continuum approach is followed. Only one species of cations (subscript +) is assumed as a mobile charge carrier within a stationary anion (subscript −) lattice. This corresponds to a transference number t_+ of one and is a valid assumption for various commonly used solid electrolyte materials.³⁰ We refer to the cation concentration as c_+ , with $c_+ \in]0, c_{+, \max}[$. The motion of the cations is expressed by the flux vector N_+ . Thus, the conservation of cations is ensured by

$$\frac{\partial c_+}{\partial t} + \nabla \cdot N_+ = 0. \quad [\text{A}\cdot 1]$$

The free charge q_F reflects the sum of all charged species and is calculated as the sum of the charge induced by the anions and the cations

$$q_F = \sum_i z_i F c_i, \quad [\text{A}\cdot 2]$$

with $i \in \{+, -\}$, F denoting the Faraday constant, and z_i representing the charge number of species i .

A spatially constant dielectric susceptibility χ can be assigned to the polarizable background lattice by neglecting any polarization of the cations. The local polarization density \mathbf{P} is therefore given by $\mathbf{P} = \epsilon_0 \chi \mathbf{E}$. Hence, the electric potential Φ can be calculated depending on the free charge q_F and the dielectric permeability $\epsilon = \epsilon_0(1 + \chi)$ as

$$-\nabla \cdot (\epsilon \nabla \Phi) = q_F. \quad [\text{A}\cdot 3]$$

Furthermore, the conservation of charge is decoupled from the conservation of mass and represents another independent equation. Both the free charge density q_F and the bound charge density $q_B = -\nabla \cdot \mathbf{P}$, which is the source of the local polarization, contribute to the total charge density q , i.e. $q = q_F + q_B$. Each of these quantities are conserved, which allows formulating the conservation of q_F and q_B

$$\frac{\partial q_{F,B}}{\partial t} + \nabla \cdot \mathbf{i}_{F,B} = 0. \quad [\text{A}\cdot 4]$$

The charge transfer inside the solid electrolyte is not just caused by a free current \mathbf{i}_F due to the redistribution of cations. Likewise, a polarization current \mathbf{i}_B related to the transport of q_B contributes to the total current density $\mathbf{i} = \mathbf{i}_F + \mathbf{i}_B$. Thereby, the current of free charge is derived as $\mathbf{i}_F = \sum_i z_i F N_i$, with $N_- = \mathbf{0}$ due to the fixed anion lattice. From Eq. A-4 and the definition of q_B it follows that $\mathbf{i}_B = \frac{\partial \mathbf{P}}{\partial t} = \frac{\partial(\epsilon_0 \chi \mathbf{E})}{\partial t}$, with $\mathbf{E} = -\nabla \Phi$. Finally, the conservation

of the total charge $\frac{\partial q}{\partial t} + \nabla \cdot \mathbf{i} = 0$ reads

$$\frac{\partial q}{\partial t} + \nabla \cdot \left(z_+ F N_+ - \epsilon_0 \chi \frac{\partial \nabla \Phi}{\partial t} \right) = 0. \quad [\text{A}\cdot 5]$$

Additionally, the conservation of linear momentum has to be satisfied. Changes of the linear momentum are caused by pressure gradients ∇p and electromagnetic forces $q_F \mathbf{E}$ and could be incorporated into a coupled electro-chemo-mechanics model for all-solid-state batteries as introduced in Ref. 45. However, time-scale considerations³⁵ suggest that inertial forces have a negligible impact compared to the remaining forces, which allows stating the conservation of linear momentum as

$$\nabla p = -q_F \nabla \Phi, \quad [\text{A}\cdot 6]$$

such that the mechanical pressure p can be post-processed. In order to close the system of equations, a constitutive law for the flux of cations, N_+ has to be specified. An approach based on the free energy guarantees a positive entropy production rate $\dot{s}_{\text{gen}}(\mathbf{x}, t) > 0$ to derive a linear relation between the gradients ∇c_+ , $\nabla \Phi$, and ∇p and the flux of cations, N_+ . By making use of the relation between ∇p and $\nabla \Phi$ in Eq. A-6, N_+ can be formulated, such that N_+ solely depends on ∇c_+ and $\nabla \Phi$, the respective diffusion coefficient D_+ , and the ionic conductivity σ . Both material parameters are a function of the cation concentration and the mobility factor \mathcal{L}_{++} (see Ref. 35)

$$\sigma = (z_+ F)^2 \mathcal{L}_{++} (1 - (c_{\text{max}} - c_+) c_+ \Delta \nu), \quad [\text{A}\cdot 7]$$

$$D_+ = \mathcal{L}_{++} RT \frac{c_{\text{max}}}{(c_{\text{max}} - c_+) c_+}, \quad [\text{A}\cdot 8]$$

with $\Delta \nu$ the difference in partial molar volumes of cations and cation sites, T the temperature, and R the universal gas constant. For the evaluation of the diffusion coefficient, we assume $c_+ = c_{+,e}$, if $c_+ < c_{+,e}$, and $c_+ = c_{\text{max}} - c_{+,e}$, if $c_+ > c_{\text{max}} - c_{+,e}$ with small values for $c_{+,e}$ to avoid divisions by zero during the nonlinear solution scheme. Finally, we summarize the system of equations

$$\frac{\partial c_+}{\partial t} + \nabla \cdot N_+ = 0 \quad \text{in } \Omega_{\text{SE}}, \quad [\text{A}\cdot 9]$$

$$\frac{\partial q}{\partial t} + \nabla \cdot \left(z_+ F N_+ - \epsilon_0 \chi \frac{\partial \nabla \Phi}{\partial t} \right) = 0 \quad \text{in } \Omega_{\text{SE}}, \quad [\text{A}\cdot 10]$$

$$-\nabla \cdot (\epsilon \nabla \Phi) = q_F \quad \text{in } \Omega_{\text{SE}}, \quad [\text{A}\cdot 11]$$

$$N_+ = -D_+ \nabla c_+ - \frac{\sigma}{z_+ F} \nabla \Phi \quad \text{in } \Omega_{\text{SE}}. \quad [\text{A}\cdot 12]$$

Appendix B. List of Symbols

The list of symbols does not include symbols with only a local scope.

Geometric quantities.—

d_{SCL}	thickness of SCL
l_i	length of domain i
\mathbf{n}	unit normal vector
\mathbf{x}	spatial coordinate
Γ_{i-j}	intersection of domains i and j
Ω_i	domain i
$\xi(\mathbf{x})$	natural coordinate of SCL domain

Constants.—

F	Faraday constant
R	universal gas constant
k_B	Boltzmann constant
ϵ_0	dielectric permeability of vacuum

Model parameters.—

c_*	concentration of species * or identifier *
D_+	diffusion coefficient of cations
\mathbf{E}	electric field
\mathbf{i}	flux of charge
$\mathbf{i}_{F,B}$	flux of free / bound charge
$\mathbf{K}_{\Psi_1, \Psi_2}^i$	derivative of residual of quantity Ψ_1 w.r.t. quantity Ψ_2 in domain i
N_+	flux of cations
\mathbf{P}	polarization density
p	pressure
Q_{SCL}	total charge in SCL
q	total charge density
$q_{F,B}$	free / bound charge density
\mathbf{R}_{Ψ}^i	residual of quantity Ψ in domain i
\dot{s}_{gen}	production rate of entropy
T	temperature
t	time
t_*	transference number of species *
z_*	charge of species *
χ	dielectric susceptibility
ϵ	dielectric permeability
Φ	electric potential
Ψ, Ψ	exemplary quantity
$\Delta \nu$	difference in partial molar volumes
σ	ionic conductivity
ρ	mass density
\mathcal{L}_{++}	mobility factor

ORCID

Stephan Sinzig  <https://orcid.org/0000-0002-4951-2993>
 Christoph P. Schmidt  <https://orcid.org/0000-0001-8504-9118>
 Wolfgang A. Wall  <https://orcid.org/0000-0001-7419-3384>

References

- J. Janek and W. G. Zeier, *Nat. Energy*, **1**, 16141 (2016).
- K. Takada, *Acta Mater.*, **61**, 759 (2013).
- Z.-H. Fu, X. Chen, and Q. Zhang, *Wiley Interdiscip. Rev.: Comput. Mol. Sci.*, **13**, e1621 (2022).
- T. Famprikis, P. Canepa, J. A. Dawson, M. S. Islam, and C. Masquelier, *Nat. Mater.*, **18**, 1278 (2019).
- O. Stern, *Zeitschrift für Elektrochemie und Angewandte Physikalische Chemie*, **30**, 508 (1924).
- K. Lehovec, *J. Chem. Phys.*, **21**, 1123 (1953).
- N. J. J. de Klerk and M. Wagemaker, *ACS Appl. Energy Mater.*, **1**, 5609 (2018).
- M. Haruta, S. Shiraki, T. Suzuki, A. Kumatani, T. Ohsawa, Y. Takagi, R. Shimizu, and T. Hitosugi, *Nano Lett.*, **15**, 1498 (2015).
- Y. Tateyama, B. Gao, R. Jaleem, and J. Haruyama, *Curr. Opin. Electrochem.*, **17**, 149 (2019).
- C. Yu, S. Ganapathy, E. R. H. van Eck, H. Wang, S. Basak, Z. Li, and M. Wagemaker, *Nat. Commun.*, **8**, 1086 (2017).
- J. Haruyama, K. Sodeyama, L. Han, K. Takada, and Y. Tateyama, *Chem. Mater.*, **26**, 4248 (2014).
- A. C. Luntz, J. Voss, and K. Reuter, *J. Phys. Chem. Lett.*, **6**, 4599 (2015).
- R. Usiskin and J. Maier, *Adv. Energy Mater.*, **11**, 2001455 (2020).
- J. Newman and K. E. Thomas-Alyea, *Electrochemical Systems* (Hoboken, New Jersey)(Wiley-Interscience) 3rd ed. (2004).
- A. Latz and J. Zausch, *Journal of Power Sources*, **196**, 3296 (2011).
- Z. Cheng, M. Liu, S. Ganapathy, C. Li, Z. Li, X. Zhang, P. He, H. Zhou, and M. Wagemaker, *Joule*, **4**, 1311 (2020).
- L. Katzenmeier, L. Carstensen, S. J. Schaper, P. Müller-Buschbaum, and A. S. Bandarenka, *Adv. Mater.*, **33**, 2100585 (2021).

18. L. Katzenmeier, S. Helmer, S. Braxmeier, E. Knobbe, and A. S. Bandarenka, *ACS Appl. Mater. Interfaces*, **13**, 5853 (2021).
19. L. Katzenmeier, L. Carstensen, and A. S. Bandarenka, *ACS Appl. Mater. Interfaces*, **14**, 15811 (2022).
20. L. Wang et al., *Nat. Commun.*, **11**, 5889 (2020).
21. Y. Nomura, K. Yamamoto, T. Hirayama, S. Ouchi, E. Igaki, and K. Saitoh, *Angew. Chem., Int. Ed.*, **58**, 5292 (2019).
22. M. Liu, S. Ganapathy, and M. Wagemaker, *Acc. Chem. Res.*, **55**, 333 (2022).
23. Q. Zhang, Y. Kong, K. Gao, Y. Wen, Q. Zhang, H. Fang, C. Ma, and Y. Du, *Sci. China: Technol. Sci.*, **65**, 2246 (2022).
24. C. Chen and X. Guo, *Acta Chim. Slov.*, **63**, 489 (2016).
25. M. Fingerle, R. Buchheit, S. Siculo, K. Albe, and R. Hausbrand, *Chem. Mater.*, **29**, 7675 (2017).
26. J. Vatamanu, D. Bedrov, and O. Borodin, *Mol. Simul.*, **43**, 838 (2017).
27. S. Stegmaier, J. Voss, K. Reuter, and A. C. Luntz, *Chem. Mater.*, **29**, 4330 (2017).
28. L. Katzenmeier, M. Gößwein, A. Gagliardi, and A. S. Bandarenka, *J. Phys. Chem. C*, **126**, 10900 (2022).
29. M. W. Swift and Y. Qi, *Phys. Rev. Lett.*, **122**, 167701 (2019).
30. M. W. Swift, J. W. Swift, and Y. Qi, *Nat. Comput. Sci.*, **1**, 212 (2021).
31. D. Brogioli, F. Langer, R. Kun, and F. L. Mantia, *ACS Appl. Mater. Interfaces*, **11**, 11999 (2019).
32. J. Lück and A. Latz, *Phys. Chem. Chem. Phys.*, **20**, 27804 (2018).
33. S. Hein et al., *J. Electrochem. Soc.*, **167**, 013546 (2020).
34. J. Lück and A. Latz, *Phys. Chem. Chem. Phys.*, **21**, 14753 (2019).
35. S. Braun, C. Yada, and A. Latz, *J. Phys. Chem. C*, **119**, 22281 (2015).
36. K. Becker-Steinberger, S. Schardt, B. Horstmann, and A. Latz, *Statics and Dynamics of Space-Charge-Layers in Polarized Inorganic Solid Electrolytes* (2021), arXiv:2101.10294.
37. J. C. Bachman et al., *J. Chem. Rev.*, **116**, 140 (2015).
38. F. Verdugo and W. A. Wall, *Comput. Methods Appl. Mech. Eng.*, **310**, 335 (2016).
39. R. Fang, P. Farah, A. Popp, and W. A. Wall, *Int. J. Numer. Methods Eng.*, **114**, 1411 (2018).
40. R. Fang, M. Kronbichler, M. Wurzer, and W. A. Wall, *Comput. Methods Appl. Mech. Eng.*, **350**, 803 (2019).
41. BACI, "A Comprehensive Multi-Physics Simulation Framework, accessed: January 14, 2023." <https://baci.pages.gitlab.lrz.de/website/>. (2023).
42. W. J. Kwon, H. Kim, K.-N. Jung, W. Cho, S. H. Kim, J.-W. Lee, and M.-S. Park, *J. Mater. Chem. A*, **5**, 6257 (2017).
43. W. Bucheli, K. Arbi, J. Sanz, D. Nuzhnyy, S. Kamba, A. Várez, and R. Jimenez, *Phys. Chem. Chem. Phys.*, **16**, 15346 (2014).
44. H. Jena, K. V. G. Kutty, and T. R. N. Kutty, *J. Mater. Sci.*, **40**, 4737 (2005).
45. C. P. Schmidt, S. Sinzig, V. Gravemeier, and W. A. Wall, *A Three-Dimensional Finite Element Formulation Coupling Electrochemistry and Solid Mechanics on Resolved Microstructures of All-Solid-State Lithium-Ion Batteries* (2022), <https://ssrn.com/abstract=4189627>.